# Diffuse interface model for cell interaction and aggregation with Lennard-Jones type potential

Shen, Lingyue; Lin, Ping; Xu, Zhiliang; Xu, Shixin

*Published in:*
Computer Methods in Applied Mechanics and Engineering

*DOI:*
10.1016/j.cma.2023.116257

*Publication date:*
2023

# Diffuse Interface Model for Cell Interaction and Aggregation with Lennard-Jones Type Potential

Lingyue Shen[1], Ping Lin[1], Zhiliang Xu[2], and Shixin Xu*[3]

[1] *Department of Mathematics University of Dundee Dundee DD1 4HN*
[2] *Department of Applied and Computational Mathematics and Statistics, University of Notre Dame,102G Crowley Hall, Notre Dame, IN 46556, US*
[3] *Zu Chongzhi Center for Mathematics and Computational Sciences (CMCS), Global Health Research Center (GHRC), Duke Kunshan University, 8 Duke Ave., Kunshan, Jiangsu, 215316, China*

**Abstract**

This study introduces a phase-field model designed to simulate the interaction and aggregation of multicellular systems under flow conditions within a bounded spatial domain. The model incorporates a multi-dimensional Lennard-Jones potential to account for short-range repulsion and adhesive bonding between cells. To solve the governing equations while preserving energy law, a second-order accurate $C^0$ finite element method is employed. The validity of the model is established through numerical tests, and experimental data from cell stretch tests is utilized for model calibration and validation. Additionally, the study investigates the impact of varying adhesion properties in red blood cells. Overall, this work presents a thermodynamically consistent and computationally efficient framework for simulating cell-cell and cell-wall interactions under flow conditions.

***Keywords***— Cell interaction; aggregation; Energy-law preserving scheme

## 1 Introduction

One major type of biological cell–cell interaction is characterized by the direct interactions between cell membranes. These interactions can be purely mechanical or involve cell adhesion molecules (CAM) exposed on cell membranes [63, 10]. Two major factors that dominate such interactions are: (i) finite size effects that drive short-range repulsion (pushing) between cells to prevent them from overlapping; and (ii) adhesion (attraction) due to the formation of adhesive bonds with CAM on adjacent cell membranes [63, 10]. Cell-cell interaction is an important subject for understanding hemodynamics because structural interactions at the cellular level unambiguously appear in a broad spectrum of blood flow-related problems ranging from red blood cells (RBCs) distribution [35] in the blood vessel, the growth of blood clot [19], blood cell aggregation [36], sickle cell disease [2], tumor cell dynamics [9] and diabetes [10]. It is known that the RBCs aggregate to form rouleaux structure due to the adhesion forces between RBCs [75, 59]. Also, the interaction between blood cells and blood vessel wall is a critical initial step in responding to different diseases, such as pathological inflammation and thrombosis [61, 38, 64].

Over the past decades, a large number of mathematical models are proposed to study cell-cell interaction. In particular, some of these models are devoted to studying the plasma membranes interaction using vesicles which largely preserve the plasma membrane lipidome and proteome [60, 40]. Within the framework of sharp interface description in which interfaces separating different components of matter are idealized as hypersurfaces with zero thickness, there are a number of studies focusing on modeling cell-cell and cell-blood-vessel interactions under blood flow conditions. Following the seminal work of Peskin [48, 49], the immersed boundary method is used to develop a model for platelet aggregation [18]. Cell-wall interaction model [9] is introduced to simulate the adhesion and deformation of tumor cells at the vessel wall. Local and non-local models [20] are described to investigate the invasion and growth of tumor cells. RBC or vesicle aggregation is studied in [76, 37, 75, 74]. Multi-scale models are introduced in [16, 70] in which dissipative particle dynamics (DPD) is used in [16] to establish a blood cell in flow model, and a stochastic cellular potts model (CPM) is introduced in [70] for studying blood clot growth. To account for cell-cell or cell-substrate

adhesion, a Lennard-Jones type potential [17, 52, 53] is introduced as a one-dimensional function of the distance between the points on different cell membranes and substrates. The potential is a combination of a repulsive part and an attractive part which shows repulsion when cells get too close to each other, and shows attraction when the distance between cells increases. This potential in combination with the DPD method, is utilized to study cell deformation and doublet suspension [52].

The diffuse interface method, also commonly known as the phase-field approach [4] is another popular method to model cell-cell interaction and aggregation. The diffuse interface model replaces the sharp interface description with a thin transition region (diffuse layer) in which microscopic mixing of the macroscopically distinct components of matter is permitted. The phase-field approach has two main advantages. First, it is easy to implement for tracking interfaces in problems that evolve large deformation or topological change of the interfaces; second, phase-field models derived from the energy dissipation law can be made thermodynamically consistent. This makes designing energy-stable numerical schemes that benefit the long time numerical simulation possible [39, 4, 14, 13].

The first goal of this paper is to derive a thermodynamically consistent phase-field model for motion, interaction and aggregation of cells or vesicles under flow conditions in a closed spatial domain using an energy variational method. [57, 58, 25, 31]. By treating the cell membrane as a diffuse interface, several phase-field vesicles or cells interaction models have been reported recently. Marth et al. [40] proposed a phase-field model for RBCs and white blood cell interactions by using a Gaussian potential for short-range repulsion. [73] introduced an adhesion potential based on the distance to the substrate in the phase-field framework. Gu et al. [22] proposed a potential by using two independent phase-field functions, one simulating the deformation and adhesion process of the vesicle and the other simulating the fixed substrate. Later on, an adhesion potential using a phase-field formulation [23] is constructed to take vesicle-substrate adhesion into account. However, as previously mentioned, cells can exhibit both adhesive and repulsive behaviors simultaneously. This phenomenon is particularly evident during embryonic development, where cells must adhere to one another to form tissues and organs, while also repelling neighboring cells to establish proper boundaries and patterns. This intricate interplay between adhesion and repulsion is crucial for processes such as tissue morphogenesis, cell sorting, and organ formation. The coexistence of adhesion and repulsion enables cells to dynamically interact with their environment, regulate cell-cell contacts, and maintain tissue organization throughout various biological processes. It is important for the model to consistently consider this aspect. In order to achieve this goal, several studies have proposed models that incorporate both adhesion and repulsion. For instance, [44, 5, 3], have explored the physical and mechanical aspects of cell interactions, considering the simultaneous presence of adhesion and repulsion forces. These studies provide valuable insights into understanding the complex dynamics and behaviors exhibited by cells when both adhesive and repulsive mechanisms are at play. While the adhesion is modeled as a function of the gradient of two phases; the repulsion is modeled as a function of two phases, respectively. However, the adhesion potential in [22, 23, 44] and the repulsion potential in [44, 5] are global which means the forces exist even when two vesicles are far away from each other. Although the model described in [3] ensured that the effects of all interaction potentials are local, its adhesion term involves high-order derivatives which limit the utilization of some well-developed numerical schemes such as $C^0$ finite element schemes.

Motivated by previous works, one novel aspect of the work proposed in this paper is the introduction of a multi-dimensional Lennard-Jones (LJ) type potential within the framework of the phase-field approach for modeling the multiple cell-cell, cell-wall interactions. This new multi-dimensional LJ potential does not involve high-order derivatives, which makes it easier to design a new $C^0$ finite element scheme in numerical simulation. To the best of the authors' knowledge, this is the first time that both the short-range repulsion by cell finite size effects and cell-cell, cell-wall adhesion by CAM are taken into consideration consistently in the phase-field framework, and are implemented using a $C^0$ finite element method. All current phase-field models mainly focus on cell adhesion. Here, our idea of the multi-dimensional LJ type potential enables us to resolve these aforementioned two factors dominating cell-cell, cell-wall interaction in a consistent and simple manner.

The energy variational method [57, 58] ensures that energy dissipation law [45, 46] is satisfied. This leads to the thermodynamical consistency of the model. All the physics that ones are interested in are taken into consideration through definitions of the energy functional and the dissipation functional, together with the kinematic relations (assumptions) of the dynamic evolution of model state variables.

Numerically simulating these aforementioned phase-field models is challenging. Finite difference method [12], finite element method [24, 73, 11, 33] and spectral methods [23, 8] are proposed with different applications. Despite the fact that most phase-field models follow the energy dissipation law at the continuous level, there have been few works on developing energy-stable numerical schemes for these vesicle or cell models. A decoupled energy-stable scheme [7] is proposed for an Allen Cahn-Navier Stokes (AC-NS) model by introducing an intermediate velocity. An unconditionally energy-stable numerical scheme [24] is introduced for a Cahn Hilliard-Navier Stokes (CH-NS) system.

However, there is still room for improving these schemes. E.g., the local inextensibility of the cell membrane is not considered. The discrete energy of numerical solutions computed by these schemes decays in a manner different from the energy dissipation law at the continuous level.

The second goal of this paper is to propose an energy-law-preserving finite element scheme for solving model governing equations, the CH-NS system with the AC general Navier boundary condition (GNBC) following the idea introduced by Shen et al. [58]. There are a few typical energy-law-preserving methods such as midpoint type of schemes (See, e.g. [26, 57]), IEQ (See e.g. [56, 72]) and SAV (See e.g. [56, 55]. We shall use a midpoint type of scheme in this paper following [58]. The proposed scheme exactly preserves a discrete counterpart of the energy dissipation property of the continuum model by discretizing the nonlinear term in a specific way. We apply our model to simulate multiple cells and vesicles interacting with each other and the substrate under flow conditions *in silico*, such as RBCs passing a branched blood vessel. We also note that although this scheme is designed for solving the model equations, it can be easily adapted to other CH-NS systems.

The rest of the paper is organized as follows. In Section 2, the thermodynamically consistent model considering cell-cell and cell-wall interaction is derived, and the energy dissipation law of the model is given. In Section 3, an energy-law-preserving scheme is proposed to solve the obtained system. Section 4 is used to present the results of numerical simulations and compare them with the data collected in laboratory experiments. The conclusion is drawn in Section 5.

# 2 Model Derivation

Derivation of the model in this paper is based on the energy dissipation law which holds ubiquitously in physical and biophysical systems involving irreversible processes [66, 15, 32, 67, 28]. This law states that for an isothermal and closed system the rate of change of the energy of the system is equal to the dissipation of the energy as follows:

$$\frac{d}{dt}E^{\text{total}} = -\triangle \leq 0 \ , \tag{1}$$

where $E^{\text{total}}$ is the total energy of the system, which is the sum of the kinetic energy $\mathcal{K}$ and the Helmholtz free energy $\mathcal{F}$ of the system. $\triangle$ is the rate of energy dissipation, which in fact is the entropy production. Eq. (1) can be easily derived via the combination of the First and Second Laws of Thermodynamics.

The choices of the total energy functional and the dissipation functional, together with the kinematic (transport) assumptions of the state variables employed in the system, determine all the physical and mechanical considerations of the problem [21].

## 2.1 Multi-cell interaction System

Energy variational method [57] is adopted for model derivation to ensure the thermodynamics consistency (1) of the derived model. We refer the readers to [57, 58, 69] for detailed discussions of this method.

Figure 1 is a schematic illustration showing the setup of the model. Let the problem domain be $\Omega$, and its wall boundary be $\partial\Omega_w$. For a multi-cellular flow system, the dynamic evolution of the $i^{th}$ cell (or vesicle) under flow conditions within $\Omega$ is tracked by the phase-field function $\phi_i(\boldsymbol{x}, t)$. Notice that $\phi_i(\boldsymbol{x}, t) \in [-1, 1]$ with $\phi_i = 1$ for intracellular space and $\phi_i = -1$ for extracellular space. The membrane of the cell is identified by $\phi_i(\boldsymbol{x}, t) = 0$. We also introduce a phase-field function $\phi_w(\boldsymbol{x}) \in [-1, 1]$ to represent the wall boundary of the domain as shown in Figure 1. This is for considering cell-wall interaction described below.

**Remark 2.1.** *In the case of Figure 1, the wall effect is considered as a force inside the domain instead of a condition on the boundary. In this particular simulation, the cell is not supposed to contact the wall when moving in the domain which is consistent with the physical fact that the cell would not merge together with the wall. One thing that needs to be emphasized is that adding such an extra term does not conflict with the GNBC. So in the following derivation of the governing equation, we still keep GNBC in the boundary condition.*

We assume that the dynamical evolution of the phase-field function $\phi_i$ is a generalized gradient flow, see Eq. (2a). We also utilize the laws of conservation for describing the dynamics of the linear momentum and the total mass of the system, see Eqs. (2b)-(2c). The cell membrane (interface) is assumed to be inextensible. The equation for local inextensibility of the interface is given by Eq. (2d).

$$\frac{\partial \phi_i}{\partial t} + \nabla \cdot (\mathbf{u}\phi_i) = \nabla \cdot \mathbf{q}_{\phi_i} \ , \tag{2a}$$

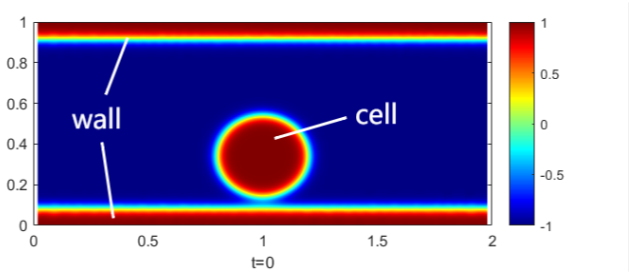


Figure 1: A schematic showing the model setup. Phase-field functions are used to represent the domain wall boundary and the cell interface, respectively. Values of the phase-field functions are indicated by the color bar.

$$\rho\left(\frac{\partial \mathbf{u}}{\partial t}+(\mathbf{u}\cdot\nabla)\mathbf{u}\right)=\nabla\cdot\boldsymbol{\sigma}_{\eta}+\mathbf{F}_{\phi_1,\phi_2,\ldots,\phi_N}\ , \tag{2b}$$

$$\nabla\cdot\mathbf{u}=0\ , \tag{2c}$$

$$(\mathcal{P}_i:\nabla\mathbf{u})\delta_i=0\ . \tag{2d}$$

Here $\rho$ is the averaged density of the system. In this work, $\rho$ is assumed to be a constant. $\mathbf{u}$ is the macroscopic velocity of the system, and $\boldsymbol{\sigma}_{\eta}$ is the system's visco-elastic stress yet to be specified.

The unidentified flux $\mathbf{q}_{\phi_i}$ in Eq. (2a) will be determined by postulating that $\phi_i$ is driven by gradients in the chemical potential. This leads to the Cahn-Hilliard equation which ensures the conservation of the volume of a cell during its dynamic evolution. $\boldsymbol{F}_{\phi_1,\phi_2,\ldots,\phi_n}$ in Eq. (2b) is the body force induced by cell-fluid interaction and is yet to be specified as well.

It has been reported that the cell membrane can be stretched by only 2–4% before rupturing [43, 34]. This membrane property is referred to as the local inextensibility of the membrane [58, 1]. Equation (2d) is the diffuse interface approximation of the local inextensibility of the membrane of the $i^{th}$ cell . $\delta_i=\frac{1}{2}\gamma^2|\nabla\phi_i|^2$ is the surface delta function with the diffuse interface thickness $\gamma$. $\mathcal{P}_i$ is the projection operator, and is defined to be $(I-\mathbf{n}_{i,m}\otimes\mathbf{n}_{i,m})$. $\mathbf{n}_{i,m}=\frac{\nabla\phi_i}{|\nabla\phi_i|}$ is the unit outward normal vector of the interface when it is defined as an implicit surface by the phase-field function. This equation is equivalent to

$$\mathcal{P}_i:\nabla\mathbf{u}=0$$

in the case of sharp interface description of the model problem. In the phase-field framework, $\mathcal{P}_i:\nabla\mathbf{u}=0$ is extended to the whole domain by multiplying the scalar function $\delta_i$ [57] for the convenience of computation.

Following the idea introduced in [1, 58], here we add a relaxation term $\xi\gamma^2\nabla\cdot(\phi_i^2\nabla\lambda_i)$ in Eq. (2d) where $\xi$ is a parameter independent of $\gamma$, and $\lambda_i$ is a function that measures the interface "pressure" induced by the inextensibility of the membrane of the $i^{th}$ cell. Thus Eq. (2d) is revised to be:

$$(\mathcal{P}_i:\nabla\mathbf{u})\delta_i+\xi\gamma^2\nabla\cdot(\phi_i^2\nabla\lambda_i)=0 \tag{3}$$

Eqs. (2a)-(2c) and (3) together constitute the governing equations of the model.

The wall boundary conditions on the top and bottom of the domain, denoted by $\partial\Omega_w$, are given as follows:

$$\begin{cases}\mathbf{u}\cdot\mathbf{n}=0\ ,\\ \mathbf{u}_{\tau}\cdot\boldsymbol{\tau}_k=f_{\boldsymbol{\tau}_k}\ ,\\ \frac{\partial\phi_i}{\partial t}+\mathbf{u}\cdot\nabla_{\Gamma}\phi_i=J_{\Gamma_i}\ ,\\ \mathbf{q}_{\phi_i}\cdot\mathbf{n}=0\ .\end{cases} \tag{4}$$

On the boundary $\partial\Omega_w$, an Allen-Cahn $(4)_3$ type boundary condition is employed for $\phi_i$. $\nabla_{\Gamma}=\nabla-\mathbf{n}(\mathbf{n}\cdot\nabla)$ is the surface gradient operator, and $\mathbf{u}_{\tau}=\mathbf{u}-(\mathbf{u}\cdot\mathbf{n})\mathbf{n}$ is the fluid slip velocity with respect to the wall where $\boldsymbol{\tau}_i, i=1,2$ are the tangential directions of the wall surface. $\mathbf{n}$ is the unit outward normal vector of the wall. $f_{\boldsymbol{\tau}_i}$ is the slip velocity of the fluid on the wall along the $\boldsymbol{\tau}_i$ direction. $J_{\Gamma}$ represents the Allan-Cahn type of relaxation on the wall by using the phase-field method and is yet to be identified. We note that these boundary conditions are also used in [50, 57].

The total energy functional $E_{total}$ of the multi-cellular system is assumed to be the sum of the kinetic energy $E_{kin}$ in the macroscale, elastic energy $E_{cell}$ of the cell membranes, cell-cell interaction energy $E_{int}$ and cell-wall adhesion energy $E_w$ in the microscale. Therefore

$$\begin{aligned} E_{total} &= \underbrace{E_{kin}}_{Macroscale} + \underbrace{E_{cell} + E_{int} + E_w}_{Microscale} \\ &= \int_\Omega \left(\frac{1}{2}\rho|\mathbf{u}|^2\right) d\boldsymbol{x} + \sum_{i=1}^{N} \int_\Omega \frac{\hat{\kappa}_B}{2\gamma} \left|\frac{f(\phi_i)}{\gamma}\right|^2 d\boldsymbol{x} + \sum_{i=1}^{N} \frac{\mathcal{M}_s}{2} \frac{(S(\phi_i(t)) - S(\phi_i(t=0)))^2}{S(\phi_i(t=0))} \\ &+ \int_\Omega H d\boldsymbol{x} + \sum_{i=1}^{N} \int_\Omega f_w(\phi_i) ds \ . \end{aligned} \tag{5}$$

The $E_{cell}$ consists of an elastic energy $\sum_{i=1}^{N} \int_\Omega \frac{\hat{\kappa}_B}{2\gamma} \left|\frac{f(\phi_i)}{\gamma}\right|^2 d\boldsymbol{x}$ and a penalty $\sum_{i=1}^{N} \frac{\mathcal{M}_s}{2} \frac{(S(\phi_i(t)) - S(\phi_i(t=0)))^2}{S(\phi_i(t=0))}$ for globally conserving surface areas of the cells. $\hat{\kappa}_B$ is the bending modulus of the membrane, and $\gamma$ is the thickness of the diffuse interface representation of the cell membrane. The membrane elastic energy density is given by

$$f(\phi_i) = \frac{\delta G}{\delta \phi_i} = -\gamma^2 \Delta \phi_i + (\phi_i^2 - 1)\phi_i \ , \tag{6}$$

with

$$G(\phi_i) = \frac{\gamma^2 |\nabla \phi_i|^2}{2} + \frac{(1 - \phi_i^2)^2}{4} \ . \tag{7}$$

The function $S(\phi_i) = \int_\Omega \frac{G(\phi_i)}{\gamma} dx$ is used to measure the surface area of the cell [1, 14, 57]. $\mathcal{M}_s$ is the penalty constant.

The term $H$ denotes the interaction energy density induced by the interaction of cells. There are many different previous works to define interaction potential $H$. See [23, 33, 71].

Here we begin with considering mechanical interaction between two cells identified by phase-field functions $\phi_1$ and $\phi_2$, respectively. Recall that $\phi_i = 1$ represents the intracellular space, and $\phi_i = -1$ represents the extracellular space of the $i^{\text{th}}$ cell, respectively. Whether there exists mechanical interaction between the two cells can be determined by measuring the overlap (i.e., occupying the same physical space) of the intracellular spaces of these two cells. To account for adhesion and repulsion between $\phi_1$ and $\phi_2$, we propose the following multi-dimensional Lennard-Jones type interaction energy density

$$H_{12} = Q_1(\phi_1 + 1)^2(\phi_2 + 1)^2 - Q_2(\phi_1^2 - 1)^2(\phi_2^2 - 1)^2 \ . \tag{8}$$

The first term in Eq. (8) accounts for the repulsion and achieves the maximum when two cells overlap at a spatial location $\boldsymbol{x}$, i.e., $\phi_1(\boldsymbol{x}) = \phi_2(\boldsymbol{x}) = 1$. The second term represents the adhesion, and is nonzero only when the diffuse layers representing the membranes of the two cells overlap, i.e., at the location of overlap $\boldsymbol{x}$, $-1 < \phi_1(\boldsymbol{x}) < 1$ and $-1 < \phi_2(\boldsymbol{x}) < 1$. This is used to mimic the adhesive interaction mediated by forming adhesive bonds with CAM on adjacent cell membranes, or via forming binding bonds between CAM and cell-extracellular matrix. In the real world, the formation and dissociation of the bonds are stochastic in nature and depend on the concentrations of agonists [29, 10]. Here we let the $Q_1$ and $Q_2$ be constants for simplicity. We note that the formation and dissociation of binding bonds occur on an order of micro-second time scale. And our model concerns the dynamics of cells on a second order time scale. Thus it is reasonable to neglect the stochastic effects of CAM binding.

Figure 2 plots the energy landscape of the interaction potential at a spatial point due to the presence of the phases $\phi_1$ and $\phi_2$. The energy is equal to 0 when these two phases do not touch or overlap i.e., $\phi_1(\mathbf{x}) = \phi_2(\mathbf{x}) = -1$. When they start to overlap, the energy first decreases, which means that the attraction force between these two phases dominates. Then the energy increases, which indicates the repulsive force dominates. This prevents the two phases from occupying the same physical space. So the interacting potential energy behaves conceptually similar to a Lennard-Jones potential. We remark that in [22] a potential of the form $(\phi_1^2 - 1)^2(\phi_2^2 - 1)$ is used, where only attractive force is included.

Generalization of $H_{12}$ for the multiple cell interactions leads to the following interaction energy density definition:

$$H = \sum_{i=1}^{N} \sum_{i<j} H_{ij} = \sum_{i=1}^{N} \sum_{i<j} \left[Q_1(\phi_i + 1)^2(\phi_j + 1)^2 - Q_2(\phi_i^2 - 1)^2(\phi_j^2 - 1)^2\right] . \tag{9}$$

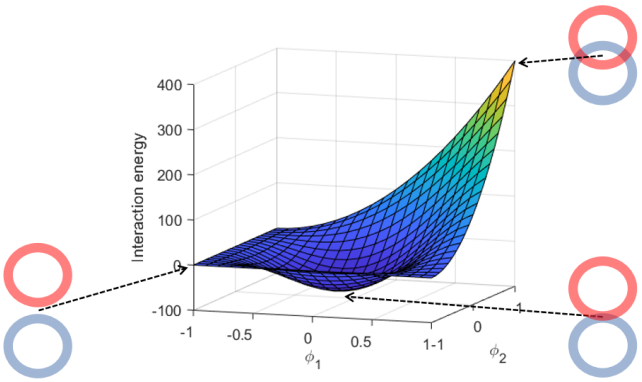


Figure 2: Interaction energy with respect to $\phi_1$ and $\phi_2$ at a space point. The energy status of different overlapping condition of the cell phase at the point are pointed out as well. ( $Q_1 = 50$, $Q_2 = 400$. )

Notice that Eq.(9) is consistent with [3] when the system reaches thermodynamic equilibrium. This also proves the feasibility of our model. Following the above interaction potential definition, the cell-wall interaction energy density is defined by setting $\phi_2 \equiv \phi_w$ in Eq. (8),

$$f_w(\phi_i) = Q_{w_1}(\phi_i + 1)^2(\phi_w + 1)^2 - Q_{w_2}(\phi_i^2 - 1)^2(\phi_w^2 - 1)^2 \ , \tag{10}$$

where $Q_{w_1}$ is repulsive energy density coefficient and $Q_{w_2}$ is adhesion energy density coefficient. Notice that the cell-wall energy $E_w$ is defined on the bulk region of the domain, and is not on the boundary. $f_w$ is non-zero only when the two phases $\phi_i$ and $\phi_w$ overlap. This can be interpreted as that the attraction force is present only when the cell makes contact with (or is close enough to) the wall, and the binding bond is formed.

With the total energy of the system given, the chemical potential $\mu_i$ for each phase $\phi_i$ is calculated as follows

$$\begin{aligned} \mu_i &= \frac{\delta(E_{cell} + E_{int} + E_w)}{\delta\phi_i} \\ &= \frac{\hat{\kappa}_B}{\gamma^3} g(\phi_i) + \frac{\mathcal{M}_s}{\gamma} \frac{S(\phi_i) - S(\phi_{i,0})}{S(\phi_{i,0})} f(\phi_i) + \frac{\partial H}{\partial \phi_i} + \frac{\partial f_w(\phi_i)}{\partial \phi_i} \ , \end{aligned} \tag{11}$$

where $g(\phi_i) = -\gamma^2 \Delta f(\phi_i) + (3\phi_i^2 - 1) f(\phi_i)$.

The dissipation functional of the system consists of the dissipation introduced by fluid viscosity, friction near the wall, and interfacial mixing due to the diffuse interface representation [58]:

$$\begin{aligned} \Delta &= \int_\Omega 2\eta |\boldsymbol{D}_\eta|^2 d\boldsymbol{x} + \sum_{i=1}^N \int_\Omega \frac{1}{M_\phi} |q_{\phi_i}|^2 d\boldsymbol{x} + \int_{\partial\Omega_w} \beta_s |\mathbf{u}_{\boldsymbol{\tau}}|^2 ds \\ &\quad + \sum_{i=1}^N \left( \int_{\partial\Omega_w} \kappa_\Gamma |J_{\Gamma_i}|^2 ds + \int_\Omega \xi |\gamma\phi_i \nabla\lambda_i|^2 dx \right) \ , \end{aligned} \tag{12}$$

where $\boldsymbol{D}_\eta = \frac{\nabla\mathbf{u} + (\nabla\mathbf{u})^T}{2}$, $\eta$ is the viscosity of the fluid, $\beta_s$ is the fluid-wall friction coefficient, $M_\phi$ and $\kappa_\Gamma$ are the mobility of the phases on the bulk and the boundary of the domain. We note that in general, the viscosity $\eta$ could be a function of all phase-field phases $\eta = \eta(\phi_w, \phi_1, \cdots, \phi_n)$ .

The specific expressions of the flux and stress functions in the kinematic equations (2a)-(2c), (3) and (4) are obtained by taking the time derivative of the total energy functional and comparing with the defined dissipation functional. The time derivative of the total energy goes:

$$\begin{aligned} \frac{dE_{total}}{dt} &= \frac{d}{dt} E_{kin} + \frac{d}{dt} E_{cell} + \frac{d}{dt} E_w \\ &\equiv I_1 + I_2 + I_3 \ . \end{aligned} \tag{13}$$

Taking the time derivative of $E_{kin}$, together with the conservation law of momentum (2b), incompressibility of the fluid (2c) and local inextensibility of the membrane (3) yields

$$\begin{aligned}
I_1 &= \frac{d}{dt}\int_\Omega \frac{\rho|\mathbf{u}|^2}{2}d\boldsymbol{x} \\
&= \int_\Omega \frac{1}{2}\frac{\partial \rho}{\partial t}|\mathbf{u}|^2 d\boldsymbol{x} + \int_\Omega \rho\frac{d\mathbf{u}}{dt}\cdot\mathbf{u}d\boldsymbol{x} + \int_\Omega \nabla\cdot(\rho\mathbf{u})\frac{|\mathbf{u}|^2}{2}d\boldsymbol{x} \\
&= \int_\Omega (\nabla\cdot\boldsymbol{\sigma}_\eta)\cdot\mathbf{u}d\boldsymbol{x} + \int_\Omega \mathbf{F}\cdot\mathbf{u}d\boldsymbol{x} + \sum_{i=1}^N\int_\Omega \lambda_i\delta_i\mathcal{P}_i : \nabla\mathbf{u}d\boldsymbol{x} \\
&\quad + \sum_{i=1}^N\int_\Omega \xi\gamma^2\lambda_i\nabla\cdot(\phi_i^2\nabla\lambda_i)d\boldsymbol{x} - \int_\Omega pI : \nabla\mathbf{u}d\boldsymbol{x} \\
&= -\int_\Omega ((\boldsymbol{\sigma}_\eta + pI) : \nabla\mathbf{u})d\boldsymbol{x} + \int_\Omega \mathbf{F}\cdot\mathbf{u}dx - \sum_{i=1}^N\int_\Omega \nabla\cdot(\lambda_i\delta_i\mathcal{P}_i)\cdot\mathbf{u}d\boldsymbol{x} \\
&\quad - \sum_{i=1}^N\int_\Omega \xi\gamma^2\phi_i^2(\nabla\lambda_i)^2 d\boldsymbol{x} + \int_{\partial\Omega_w}((\boldsymbol{\sigma}_\eta + \sum_{i=1}^N\lambda_i\delta_i\mathcal{P}_i)\cdot\mathbf{n})\cdot\mathbf{u}_\tau dS\ ,
\end{aligned} \tag{14}$$

where the slip boundary condition is used. Here the pressure $p$ is a Lagrangian multiplier and is introduced to ensure the incompressibility of the fluid.

Taking the time derivative of $E_{cell}$ together with the transport assumption of each field-phase phase representing cells (2a) yields

$$\begin{aligned}
I_2 &= \frac{d}{dt}\int_\Omega \frac{\hat{\kappa}_B}{2\gamma}\sum_{i=1}^N\left|\frac{f(\phi_i)}{\gamma}\right|^2 d\boldsymbol{x} + \frac{d}{dt}\int_\Omega H d\boldsymbol{x} + \sum_{i=1}^N\frac{d}{dt}\frac{\mathcal{M}_s}{2}\frac{(S(\phi_i)-S(\phi_{i,0}))^2}{S(\phi_{i,0})} \\
&= \int_\Omega \frac{\hat{\kappa}_B}{\gamma}\sum_{i=1}^N\frac{f_i}{\gamma^2}\left(-\gamma^2\Delta\left(\frac{\partial\phi_i}{\partial t}\right) + (3\phi_i^2-1)\frac{\partial\phi_i}{\partial t}\right)d\boldsymbol{x} + \int_\Omega\sum_{i=1}^N\frac{\partial H}{\partial\phi_i}\frac{\partial\phi_i}{\partial t}d\boldsymbol{x} \\
&\quad + \sum_{i=1}^N\frac{d}{dt}\frac{\mathcal{M}_s}{2}\frac{(S(\phi_i)-S(\phi_{i,0}))^2}{S(\phi_{i,0})} \\
&= \int_\Omega \frac{\hat{\kappa}_B}{\gamma^3}\sum_{i=1}^N\left(-\gamma^2\Delta f_i + (3\phi_i^2-1)f_i + \frac{\partial H}{\partial\phi_i} + \frac{\mathcal{M}_s}{\gamma}\frac{S(\phi_i)-S(\phi_{i,0})}{S(\phi_{i,0})}f(\phi_i)\right)\frac{\partial\phi_i}{\partial t}d\boldsymbol{x} \\
&\quad - \int_{\partial\Omega_w}\frac{\hat{\kappa}_B}{\gamma}\sum_{i=1}^N f_i\frac{\partial}{\partial t}(\partial_n\phi_i)ds + \int_{\partial\Omega_w}\frac{\hat{\kappa}_B}{\gamma}\sum_{i=1}^N\partial_n f_i\frac{\partial\phi_i}{\partial t}ds \\
&\quad + \sum_{i=1}^N\int_{\partial\Omega_w}\mathcal{M}_s\frac{S(\phi_i)-S(\phi_{i,0})}{S(\phi_{i,0})}\gamma\partial_n\phi_i\frac{\partial\phi_i}{\partial t}ds \\
&= \sum_{i=1}^N\left(\int_\Omega \mu_i\frac{\partial\phi_i}{\partial t}d\boldsymbol{x} + \int_{\partial\Omega_w}\frac{\hat{\kappa}_B}{\gamma}f_i\frac{\partial}{\partial t}(\partial_n\phi_i)ds + \int_{\partial\Omega_w}\mathcal{M}_s\frac{S(\phi_i)-S(\phi_{i,0})}{S(\phi_{i,0})}\gamma\partial_n\phi_i\frac{\partial\phi_i}{\partial t}ds\right) \\
&= \sum_{i=1}^N\left(-\int_\Omega q_{\phi_i}\cdot\nabla\mu_i d\boldsymbol{x} - \int_\Omega \mu_i\mathbf{u}\cdot\nabla\phi_i d\boldsymbol{x} + \int_{\partial\Omega_w}\frac{\hat{\kappa}_B}{\gamma}\partial_n f_i\frac{\partial\phi_i}{\partial t}ds\right. \\
&\quad \left. + \int_{\partial\Omega_w}\mathcal{M}_s\frac{S(\phi_i)-S(\phi_{i,0})}{S(\phi_{i,0})}\gamma\partial_n\phi_i\frac{\partial\phi_i}{\partial t}ds\right)\ ,
\end{aligned} \tag{15}$$

where the Allan-Cahn boundary condition $(4)_3$ for each phase is used.

Computing $\frac{d}{dt}E_w$ yields

$$I_3 = \sum_{i=1}^N\left(\int_{\partial\Omega}\frac{\partial f_w(\phi_i)}{\partial\phi_i}\frac{\partial\phi_i}{\partial t}ds\right)\ . \tag{16}$$

By combining Eqs. (14), (15) and (16), we have:

$$\begin{aligned}\frac{d}{dt}E_{total} &= -\int_\Omega((\boldsymbol{\sigma}_\eta + pI):\nabla\mathbf{u})d\boldsymbol{x} + \int_\Omega(\mathbf{F} - \sum_{i=1}^N \mu_i\nabla\phi_i - \sum_{i=1}^N \nabla\cdot(\lambda_i\delta_i\mathcal{P}_i))\cdot\mathbf{u}d\boldsymbol{x} \\ &\quad -\sum_{i=1}^N\int_\Omega q_{\phi_i}\cdot\nabla\mu_i d\boldsymbol{x} + \sum_{i=1}^N\int_\Omega \xi\gamma^2\phi_i^2(\nabla\lambda_i)^2 d\boldsymbol{x} \\ &\quad +\int_{\partial\Omega_w}((\boldsymbol{\sigma}_\eta + \sum_{i=1}^N\lambda_i\delta_i\mathcal{P}_i)\cdot\mathbf{n} - \sum_{i=1}^N\hat{L}_i\nabla_\Gamma\phi_i)\cdot\mathbf{u}_\tau ds + \sum_{i=1}^N\int_{\partial\Omega_w}\hat{L}_i J_{\Gamma_i} ds\ ,\end{aligned} \tag{17}$$

where $\hat{L}_i = \frac{\hat{\kappa}_B}{\gamma}\partial_n f_i + \mathcal{M}_s\frac{S(\phi_i)-S(\phi_{i,0})}{S(\phi_{i,0})}\gamma\partial_n\phi_i$.

The energy dissipation law (1) is employed to close the system. In more details, we equal Eq. (17) with the negative of the energy dissipation functional defined in Eq. (12) to ensure the energy dissipation law (1) is satisfied. This gives rise to the following definitions of the flux and stress functions in the kinematic relations (2a)-(2c), (3) and (4).

$$\begin{cases}\boldsymbol{\sigma}_\eta = 2\eta\boldsymbol{D}_\eta - pI\ , & \text{in } \Omega\ , \\ q_{\phi_j} = M_{\phi_j}\nabla\mu_j\ , & \text{in } \Omega\ , \\ \mathbf{F} = \sum_{i=1}^N(\mu_i\nabla\phi_i + \nabla\cdot(\lambda_i\delta_i\mathcal{P}_i))\ , & \text{in } \Omega\ , \\ J_{\Gamma_i} = -\kappa_{\Gamma_i}^{-1}\hat{L}_i\ , & \text{on } \partial\Omega_w\ , \\ u_{\tau_j} = \beta_s^{-1}(-(\mathbf{n}\cdot(\boldsymbol{\sigma}_\eta + \sum_{i=1}^N\lambda_i\delta_i\mathcal{P}_i)\cdot\boldsymbol{\tau}_j) + \sum_{i=1}^N\hat{L}_i\partial_{\tau_j}\phi_i)\ ,\ j=1,2, & \text{on } \partial\Omega_w\ .\end{cases} \tag{18}$$

The viscosity, length, velocity, time, bulk, and boundary chemical potentials in the equations are scaled by their corresponding characteristic values $\eta_0$, $L$, $U$, $\frac{L}{U}$, $\frac{\eta_0 U}{L}$ and $\eta_0 U$, respectively. Write $Q_{w_1}, Q_{w_2}, Q_1, Q_2$ into $Q_0 q_{w_1}, Q_0 q_{w_2}.Q_0 q_1, Q_0 q_2$, where $Q_0$ is the character energy density. To this end, the proposed diffuse interface model for describing the cell-wall, cell-cell interaction, and aggregation in dimensionless form is composed of the following equations:

$$\begin{cases}Re(\frac{\partial\mathbf{u}}{\partial t} + (\mathbf{u}\cdot\nabla)\mathbf{u}) + \nabla P = \nabla\cdot(2\eta\boldsymbol{D}) + \sum_i\mu_i\nabla\phi_i + \sum_i\nabla\cdot(\lambda_i\delta_{\epsilon_i}\mathcal{P}_i)\ , & \text{in } \Omega\ , \\ \nabla\cdot\mathbf{u} = 0\ , & \text{in } \Omega\ , \\ \frac{\partial\phi_i}{\partial t} + \mathbf{u}\cdot\nabla\phi_i = -\mathcal{M}\Delta\mu_i\ , & \text{in } \Omega\ , \\ \mu_i = \kappa_B g(\phi_i) + \mathcal{M}_s\frac{(S(\phi_i)-S(\phi_{i,0}))}{S(\phi_{i,0})}f_i + \alpha\frac{\partial H}{\partial\phi_i} + \alpha\frac{\partial f_w(\phi_i)}{\partial\phi_i}\ , & \text{in } \Omega\ , \\ f_i = -\epsilon\Delta\phi_i + \frac{(\phi_i^2-1)}{\epsilon}\phi_i,\ g(\phi_i) = -\Delta f_i + \frac{1}{\epsilon^2}(3\phi_i^2-1)f_i\ , & \text{in } \Omega\ , \\ \delta_{\epsilon_i}(\mathcal{P}_i:\nabla\mathbf{u}) + \xi\varepsilon^2\nabla\cdot(\phi_i^2\nabla\lambda_i) = 0\ , & \text{in } \Omega\ ,\end{cases} \tag{19}$$

with the boundary conditions

$$\begin{cases}\kappa\dot{\phi}_i + L(\phi_i) = 0\ , & \text{on } \partial\Omega_w\ , \\ L(\phi_i) = \kappa_B\partial_n f(\phi_i) + \epsilon\mathcal{M}_s\frac{S(\phi_i)-S(\phi_{i,0})}{S(\phi_{i,0})}\partial_n\phi_i\ , & \text{on } \partial\Omega_w\ , \\ -l_s^{-1}u_{\tau_i} = \boldsymbol{\tau_i}\cdot(2\eta\mathbf{D}_\eta + \sum_i\lambda_i\delta_{\epsilon_i}\mathcal{P}_i)\cdot\boldsymbol{n} - \sum_i L(\phi_i)\partial_{\tau_i}\phi_i\ ,\ i=1,2, & \text{on } \partial\Omega_w\ , \\ f_i = 0\ , & \text{on } \partial\Omega_w\ , \\ \partial_n\mu_i = 0\ , & \text{on } \partial\Omega_w\ , \\ \partial_n\lambda_i = 0\ , & \text{on } \partial\Omega_w\ ,\end{cases} \tag{20}$$

where $S(\phi_i) = \int_\Omega\frac{\epsilon}{2}|\nabla\phi_i|^2 + \frac{1}{4\epsilon}(\phi_i^2-1)^2 d\boldsymbol{x}$ and $\delta_{\epsilon_i} = \frac{1}{2}\epsilon^2|\nabla\phi_i|^2$.

The dimensionless constants appeared in Eqs. (19)-(20) are given by $\epsilon = \frac{\gamma}{L}$, $Re = \frac{\rho_0 UL}{\eta_0}$, $\mathcal{M} = \frac{M_\phi\eta_0}{L^2}$, $\kappa_B = \frac{\hat{\kappa}_B}{L^2\eta_0 U}$, $k = \frac{\hat{\kappa}_B}{\eta_0 L}$, $l_s = \frac{\eta_0}{\beta_s L}$, $\alpha = \frac{Q_0}{\eta_0 U}$, $\mathcal{M}_s = \frac{M_s}{\eta_0 U}$.

# 3 Energy-law-preserving Scheme

We define the Sobolev spaces as follows [27, 57]

$$
\begin{aligned}
\boldsymbol{W}^{1,3} &= (W^{1,3})^2 \ , \\
\boldsymbol{W}_N^{1,\frac{3}{2}} &= (W^{1,\frac{3}{2}})^N \ , \\
\boldsymbol{W}_N^{1,3} &= (W^{1,3})^N \ , \\
\boldsymbol{W}_N^{1,\frac{3}{2}}(\Omega) &= \left\{ \Lambda = (\lambda_1, \lambda_2, ...\lambda_N)^T \right\} \ , \\
\boldsymbol{W}^{1,3}(\Omega) &= \left\{ \mathbf{u} = (u_x, u_y)^T \in \boldsymbol{W}^{1,3} | \mathbf{u} \cdot \boldsymbol{n} = 0, \text{ on } \partial\Omega_w \right\} \ , \\
\boldsymbol{W}_\Phi^{1,3}(\Omega) &= \left\{ \Phi = (\phi_1, \phi_2, ...\phi_N)^T \in \boldsymbol{W}_N^{1,3} | -1 \le \phi_i \le 1, i = 1, 2, ...N, \text{ in } \Omega \right\} \ , \\
\boldsymbol{W}_{\boldsymbol{U}}^{1,3}(\Omega) &= \left\{ \boldsymbol{U} = (\mu_1, \mu_2, ...\mu_N)^T \in \boldsymbol{W}_N^{1,3} | \partial_n \mu_i = 0, i = 1, 2, ...N, \text{ on } \partial\Omega_w \right\} \ , \\
\boldsymbol{W}_F^{1,3}(\Omega) &= \left\{ F = (f_1, f_2, ...f_N)^T \in \boldsymbol{W}_N^{1,3} | f_i = 0, i = 1, 2, ...N, \text{ on } \partial\Omega_w \right\} \ , \\
\boldsymbol{W}_b &= \boldsymbol{W}_\Phi^{1,3}(\Omega) \times \boldsymbol{W}_F^{1,3}(\Omega) \times \boldsymbol{W}_{\boldsymbol{U}}^{1,3}(\Omega) \times \boldsymbol{W}_N^{1,\frac{3}{2}}(\Omega) \times W^{1,\frac{3}{2}}(\Omega) \times \boldsymbol{W}^{1,3}(\Omega) \ ,
\end{aligned}
$$

and let $\|\cdot\| = \left(\int_\Omega |\cdot|^2 d\boldsymbol{x}\right)^{\frac{1}{2}}$ and $\|\cdot\|_w = \left(\int_{\partial\Omega_w} |\cdot|^2 ds\right)^{\frac{1}{2}}$ denote the $L^2$ norm defined in the domain and on the domain boundary respectively.

**Theorem 3.1.** *If* $(\Phi,\ F,\ \boldsymbol{U},\ \lambda,\ P,\ \mathbf{u}) \in \boldsymbol{W}_b$ *are smooth solutions of the above system (19)-(20), the following energy law holds:*

$$
\begin{aligned}
\frac{d}{dt}\mathcal{E}_{total} &= \frac{d}{dt}(\mathcal{E}_{kin} + \mathcal{E}_{cell} + \mathcal{E}_w) \qquad (21) \\
&= \frac{1}{Re}\left( -2\|\eta^{1/2}\mathbf{D}_\eta\|^2 - \mathcal{M}\sum_i \|\nabla\mu_i\|^2 - \xi\sum_i \|\epsilon\phi_i\nabla\lambda_i\|^2 - \kappa\sum_i \|\dot{\phi}_i\|_w^2 - \|l_s^{-1/2}\mathbf{u}_\tau\|_w^2 \right) \ ,
\end{aligned}
$$

*where* $\mathcal{E}_{total} = \mathcal{E}_{kin} + \mathcal{E}_{cell} + \mathcal{E}_w$, $\mathcal{E}_{kin} = \frac{1}{2}\int_\Omega |\mathbf{u}|^2 d\boldsymbol{x}$, $\mathcal{E}_{cell} = \frac{\kappa_B}{2Re\epsilon}\sum_i \int_\Omega |f_i|^2 d\boldsymbol{x} + \mathcal{M}_s \sum_i \frac{(S(\phi_i) - S(\phi_{i,0}))^2}{2ReS(\phi_{i,0})} + \frac{\alpha}{Re}\int_\Omega H d\boldsymbol{x}$ *and* $\mathcal{E}_w = \frac{\alpha}{Re}\sum_i \int_\Omega f_w(\phi_i) d\boldsymbol{x}$.

*Proof.* Multiplying the first equation in Eq. (19) with $\mathbf{u}$ and integration by parts yield

$$
\begin{aligned}
\frac{d}{dt}\mathcal{E}_{kin} &= \frac{1}{Re}\left\{ -\int_\Omega 2\eta|\boldsymbol{D}_\eta|^2 d\boldsymbol{x} + \int_{\partial\Omega_w} (\boldsymbol{\sigma}_\eta \cdot \mathbf{n}) \cdot \mathbf{u}_\tau ds + \sum_i \int_\Omega \mu_i \nabla\phi_i \cdot \mathbf{u} d\boldsymbol{x} \right. \\
&\quad \left. - \sum_i \int_\Omega \lambda_i \delta_{\epsilon_i} \mathcal{P}_i : \nabla\mathbf{u} d\boldsymbol{x} + \sum_i \int_{\partial\Omega_w} (\lambda_i \delta_{\epsilon_i} \mathcal{P}_i \cdot \mathbf{n}) \cdot \mathbf{u}_\tau ds \right\} \\
&= \frac{1}{Re}\left\{ -\int_\Omega 2\eta|\boldsymbol{D}_\eta|^2 d\boldsymbol{x} - \sum_i \int_\Omega \lambda_i \delta_{\epsilon_i} \mathcal{P}_i : \nabla\mathbf{u} d\boldsymbol{x} - l_s^{-1} \int_{\partial\Omega_w} |\mathbf{u}_\tau|^2 ds \right. \\
&\quad \left. + \sum_i \int_{\partial\Omega_w} L(\phi_i)\partial_\tau\phi \cdot \mathbf{u}_\tau ds + \sum_i \int_\Omega \mu_i \nabla\phi_i \cdot \mathbf{u} d\boldsymbol{x} \right\} \ , \qquad (22)
\end{aligned}
$$

where the slip boundary condition in Eq. (20) is applied.

Taking the inner product of the third equation in Eq. (19) with $\frac{\mu_i}{Re}$ and summing up with respect to $i$ result in

$$
\frac{1}{Re}\sum_i \int_\Omega \frac{\partial\phi_i}{\partial t}\mu_i d\boldsymbol{x} + \frac{1}{Re}\sum_i \int_\Omega \mathbf{u} \cdot \nabla\phi_i \mu_i d\boldsymbol{x} = -\frac{1}{Re}\mathcal{M}\sum_i \int_\Omega |\nabla\mu_i|^2 d\boldsymbol{x} \ , \qquad (23)
$$

where $\partial_n\mu_i = 0$ is considered here.

Multiplying the fourth equation in Eq. (19) with $\frac{1}{Re}\frac{\partial \phi_i}{\partial t}$ and integration by parts give rise to

$$
\begin{aligned}
&\frac{1}{Re}\sum_i \int_\Omega \mu \frac{\partial \phi_i}{\partial t} d\boldsymbol{x} \qquad (24)\\
=\ & \frac{1}{Re}\sum_i \left\{ \kappa_B \int_\Omega g_i \frac{\partial \phi_i}{\partial t} d\boldsymbol{x} + \mathcal{M}_s \frac{S(\phi_i)-S(\phi_{i,0})}{S(\phi_{i,0})} \int_\Omega f_i \frac{\partial \phi_i}{\partial t} d\boldsymbol{x} + \alpha \int_\Omega \frac{\partial H}{\partial \phi_i}\frac{\partial \phi_i}{\partial t} d\boldsymbol{x} \alpha \int_\Omega \frac{f_w(\phi_i)}{\partial \phi_i}\frac{\partial \phi_i}{\partial t} d\boldsymbol{x} \right\}\\
=\ & \frac{\kappa_B}{Re}\sum_i \int_\Omega f_i \frac{\partial}{\partial t}\left(-\Delta \phi_i + \frac{1}{\epsilon^2}(\phi_i^3 - \phi_i)\right) d\boldsymbol{x} - \frac{\kappa_B}{Re}\sum_i \int_{\partial\Omega_w} \partial_n f_i \frac{\partial \phi_i}{\partial t} ds\\
& + \mathcal{M}_s \sum_i \frac{d}{dt}\left(\frac{(S(\phi_i)-S(\phi_{i,0}))^2}{2ReS(\phi_{i,0})}\right) - \mathcal{M}_s \sum_i \left(\frac{S(\phi_i)-S(\phi_{i,0})}{ReS(\phi_{i,0})}\right) \int_{\partial\Omega_w} \epsilon \partial_n \phi_i \frac{\partial \phi_i}{\partial t} ds\\
& + \frac{\alpha}{Re}\sum_i \int_\Omega \frac{\partial f_w(\phi_i)}{\partial \phi_i}\frac{\partial \phi_i}{\partial t} d\boldsymbol{x} + \frac{\alpha}{Re}\sum_i \int_\Omega \frac{\partial H}{\partial \phi_i}\frac{\partial \phi_i}{\partial t} d\boldsymbol{x}\\
=\ & \frac{d}{dt}\left(\kappa_B \sum_i \int_\Omega \frac{|f_i|^2}{2Re\epsilon} d\boldsymbol{x}\right) + \mathcal{M}_s \frac{d}{dt}\left(\sum_i \frac{(S(\phi_i)-S(\phi_{i,0}))^2}{2ReS(\phi_{i,0})}\right) + \frac{\alpha}{Re}\frac{d}{dt}\sum_i \int_\Omega f_w(\phi_i) d\boldsymbol{x}\\
& + \frac{\alpha}{Re}\frac{d}{dt}\int_\Omega H d\boldsymbol{x} - \sum_i \int_{\partial\Omega_w} \frac{L(\phi_i)}{Re}\frac{\partial \phi_i}{\partial t} ds\\
=\ & \frac{d}{dt}(\mathcal{E}_{cell} + \mathcal{E}_w) - \int_{\partial\Omega_w} \frac{L(\phi)}{Re}\frac{\partial \phi}{\partial t} ds\ ,
\end{aligned}
$$

where the definitions of $f(\phi)$, $g(\phi)$ and the boundary conditions of $\phi$ and $f$ are utilized.

Multiplying the last equations with $\frac{\lambda_i}{Re}$ and integration by parts and sum up by $i$ leads to

$$
\frac{1}{Re}\sum_i \int_\Omega (\lambda_i \delta_{\epsilon_i} \mathcal{P}_i) : \nabla \mathbf{u} d\boldsymbol{x} - \frac{1}{Re}\sum_i \int_\Omega \xi \varepsilon^2 \phi_i^2 (\nabla \lambda_i)^2 d\boldsymbol{x} = 0\ . \qquad (25)
$$

Finally, the energy dissipation law (21) is obtained by combining Eqs. (22), (23), (24) and (25) considering the boundary conditions in (20).

□

In the rest of this section, we propose an energy-law-preserving, second-order accurate in both space and time scheme for solving the model system (19)-(20).

## 3.1 Time-discrete primitive method

The mid-point method is utilized for the temporal discretization of Eqs. (19)-(20). Let $\Delta t$ denote the time step size, $()^{n+1}$ and $()^n$ denote the values of the variables at times $(n+1)\Delta t$ and $n\Delta t$, respectively. The semi-discrete in time scheme to solve Eqs. (19)-(20) is as follows:

$$
\begin{cases}
\frac{\mathbf{u}^{n+1}-\mathbf{u}^n}{\Delta t} + (\mathbf{u}^{n+\frac{1}{2}}\cdot\nabla)\mathbf{u}^{n+\frac{1}{2}} + \frac{1}{Re}\nabla P^{n+\frac{1}{2}} = \frac{1}{Re}\nabla\cdot(\eta^n(\nabla \mathbf{u}^{n+\frac{1}{2}} + (\nabla \mathbf{u}^{n+\frac{1}{2}})^T)) + \frac{1}{Re}\sum_i \mu_i^{n+\frac{1}{2}}\nabla\phi_i^{n+\frac{1}{2}} \\
\qquad\qquad + \sum_i \frac{1}{Re}\nabla\cdot\left(\lambda_i^{n+\frac{1}{2}}\mathcal{P}_i^n \delta_{\epsilon_i}\right)\ , \\
\nabla\cdot\mathbf{u}^{n+\frac{1}{2}} = 0\ , \\
\frac{\phi_i^{n+1}-\phi_i^n}{\Delta t} + (\mathbf{u}^{n+\frac{1}{2}}\cdot\nabla)\phi_i^{n+\frac{1}{2}} = -\mathcal{M}\Delta\mu_i^{n+\frac{1}{2}}\ , \\
\mu_i^{n+\frac{1}{2}} = \kappa_B g(\phi_i^{n+1},\phi_i^n) + \mathcal{M}_s\frac{(S(\phi_i^{n+\frac{1}{2}})-S(\phi_{0_i}))}{S(\phi_{0_i})} f(\phi_i^{n+1},\phi_i^n) + \alpha\frac{H_i^{n+1}-H_i^n}{\phi_i^{n+1}-\phi_i^n} + \alpha\frac{f_w(\phi_i^{n+1})-f_w(\phi_i^n)}{\phi_i^{n+1}-\phi_i^n}\ , \\
f_i^{n+\frac{1}{2}} = -\epsilon\Delta\phi_i^{n+\frac{1}{2}} + \frac{1}{\epsilon}((\phi_i^{n+\frac{1}{2}})^2-1)\phi_i^{n+\frac{1}{2}}\ , \\
\delta_{\epsilon_i}\mathcal{P}_i^n : \nabla\mathbf{u}^{n+\frac{1}{2}} + \xi\epsilon^2\nabla\cdot((\phi_i^n)^2\nabla\lambda_i^{n+\frac{1}{2}}) = 0\ ,
\end{cases} \qquad (26)
$$

with boundary conditions on $\partial\Omega_w$ ,

$$\begin{cases} \kappa\dot{\phi_i}^{n+\frac{1}{2}} = -L_i^{n+\frac{1}{2}} \ , \\ L_i^{n+\frac{1}{2}} = \kappa_B\partial_n f_i^{n+\frac{1}{2}} + \mathcal{M}_s\epsilon\frac{S({\phi_i}^{n+\frac{1}{2}})-S_{0_i}}{S_{0_i}}\partial_n\phi_i^{n+\frac{1}{2}} \ , \\ -l_s^{-1}u_{\tau_j}^{n+\frac{1}{2}} = \boldsymbol{\tau_j}\cdot(\eta^n(\nabla\mathbf{u}^{n+\frac{1}{2}} + (\nabla\mathbf{u}^{n+\frac{1}{2}})^T) + \sum_i \lambda_i^{n+\frac{1}{2}}\delta_{\epsilon_i}\mathcal{P}_i^n)\cdot\boldsymbol{n} - \sum_i L_i^{n+\frac{1}{2}}\partial_{\tau_j}\phi_i^{n+\frac{1}{2}} \ , \quad j=1,2, \\ f_i^{n+\frac{1}{2}} = 0 \ , \\ \partial_n\lambda_i^{n+\frac{1}{2}} = 0 \ , \end{cases} \tag{27}$$

with $(\cdot)^{n+\frac{1}{2}} = \frac{(\cdot)^n+(\cdot)^{n+1}}{2}$ and $\mathcal{P}_i^n = I - \mathbf{n}_m^n\otimes\mathbf{n}_m^n$ with $\mathbf{n}_m^n = \frac{\nabla\phi_i^n}{|\nabla\phi_i^n|}$ and

$$\begin{cases} f(\phi_i^{n+1},\phi_i^n) = -\epsilon\Delta\phi_i^{n+\frac{1}{2}} + \frac{1}{4\epsilon}((\phi_i^{n+1})^2 + (\phi_i^n)^2 - 2)(\phi_i^{n+1}+\phi_i^n) \ , \\ g(\phi_i^{n+1},\phi_i^n) = \left(-\Delta f_i^{n+\frac{1}{2}} + \frac{1}{\epsilon^2}\left((\phi_i^{n+1})^2 + (\phi_i^n)^2 + \phi_i^{n+1}\phi_i^n - 1\right) f_i^{n+\frac{1}{2}}\right) \ , \\ H_i^n = q_1(\phi_i^n+1)^2\sum_{j\neq i}\left[(\phi_j^{n+\frac{1}{2}}+1)^2\right] - q_2((\phi_i^n)^2-1)^2\sum_{j\neq i}\left[((\phi_j^{n+\frac{1}{2}})^2-1)^2\right] \ , \\ H_i^{n+1} = q_1(\phi_i^{n+1}+1)^2\sum_{j\neq i}\left[(\phi_j^{n+\frac{1}{2}}+1)^2\right] - q_2((\phi_i^{n+1})^2-1)^2\sum_{j\neq i}\left[((\phi_j^{n+\frac{1}{2}})^2-1)^2\right] \ , \\ f_w(\phi^n) = q_{w_1}(\phi_i^n+1)^2(\phi_w+1)^2 - q_{w_2}((\phi_i^n)^2-1)((\phi_w)^2-1) \ . \end{cases} \tag{28}$$

Thus we have

$$\begin{aligned} &\frac{H_i^{n+1}-H_i^n}{\phi_i^{n+1}-\phi_i^n} \\ = \ & \frac{1}{\phi_i^{n+1}-\phi_i^n}\left(q_1(\phi_i^{n+1}+1)^2\sum_{j\neq i}\left[(\phi_j^{n+\frac{1}{2}}+1)^2\right] - q_2((\phi_i^{n+1})^2-1)^2\sum_{j\neq i}\left[((\phi_j^{n+\frac{1}{2}})^2-1)^2\right]\right. \\ & \left. - q_1(\phi_i^n+1)^2\sum_{j\neq i}\left[(\phi_j^{n+\frac{1}{2}}+1)^2\right] + q_2((\phi_i^n)^2-1)^2\sum_{j\neq i}\left[(\phi_j^{n+\frac{1}{2}})^2-1\right]\right) \\ = \ & q_1(\phi_i^{n+1}+\phi_i^n+2)\sum_{j\neq i}\left[(\phi_j^{n+\frac{1}{2}}+1)^2\right] \\ & -q_2(\phi_i^{n+1}+\phi_i^n)((\phi_i^{n+1})^2+(\phi_i^n)^2-2)\sum_{j\neq i}\left[((\phi_j^{n+\frac{1}{2}})^2-1)^2\right] \end{aligned} \tag{29}$$

Similarly,

$$\begin{aligned} \frac{f_w(\phi_i^{n+1})-f_w(\phi_i^n)}{\phi_i^{n+1}-\phi_i^n} \ = \ & q_{w_1}(\phi_i^{n+1}+\phi_i^n+2)(\phi_w+1)^2 \\ & -q_{w_2}(\phi_i^{n+1}+\phi_i^n)((\phi_i^{n+1})^2+(\phi_i^n)^2-2)(\phi_w^2-1)^2 \end{aligned} \tag{30}$$

We keep using the notations $\frac{f_w(\phi_i^{n+1})-f_w(\phi_i^n)}{\phi_i^{n+1}-\phi_i^n}$ and $\frac{H(\phi_i^{n+1})-H(\phi_i^n)}{\phi_i^{n+1}-\phi_i^n}$ for convenience in later derivation.

**Remark 3.1.** *Note that the discrete scheme solving the model system is a fully coupled nonlinear algorithm. This may increase the cost of numerical simulation. Nevertheless, the energy-law-preserving scheme has to involve solving a nonlinear system to the best of the authors' efforts. Recent papers have introduced a number of linear decoupled schemes like IEQ and SAV methods. These methods could be considered in further studies.*

**Theorem 3.2.** *If $(\phi_i^n,\mu_i^n,\mathbf{u}^n,P^n)$ are smooth solutions of the above system (26)-(27), the following energy law is satisfied:*

$$\mathcal{E}_{total}^{n+1} - \mathcal{E}_{total}^n \ = \ (\mathcal{E}_{kin}^{n+1} + \sum_i^N\left[\mathcal{E}_{cell_i}^{n+1} + \mathcal{E}_{i,int}^{n+1} + \mathcal{E}_{w_i}^{n+1}\right]) - (\mathcal{E}_{kin}^n + \sum_i^N\left[\mathcal{E}_{cell_i}^n + \mathcal{E}_{i,int}^n + \mathcal{E}_{w_i}^n\right])$$

$$
\begin{aligned}
&= \frac{\triangle t}{Re}\left(-2\|(\eta^n)^{1/2}\mathbf{D}_\eta^{n+\frac{1}{2}}\|^2 - \mathcal{M}\sum_i^N \|\nabla\mu_i^{n+\frac{1}{2}}\|^2 - \xi\sum_i^N \|\ \epsilon\phi_i^n\nabla\lambda_i^{n+\frac{1}{2}}\|^2\right.\\
&\left. -\frac{1}{\kappa}\|\sum_i^N L(\phi_i^{n+\frac{1}{2}})\|_w^2 - \|l_s^{-1/2}\mathbf{u}_\tau^{n+\frac{1}{2}}\|_w^2\right)\ , \qquad (31)
\end{aligned}
$$

*where* $\mathcal{E}_{total}^n = \mathcal{E}_{kin}^n + \sum_i^N\left[\mathcal{E}_{cell_i}^n + \mathcal{E}_{i,int}^n + \mathcal{E}_{w_i}^n\right]$ *with* $\mathcal{E}_{kin}^n = \frac{1}{2}\|\mathbf{u}^n\|^2$, $\mathcal{E}_{cell_i}^n = \frac{\kappa_B\|f_i^n\|^2}{2Re\epsilon} + \mathcal{M}_s\frac{(S(\phi_i^n)-S(\phi_{i,0}))^2}{2ReS(\phi_{i,0})} + \frac{\alpha}{Re}H_i^n$ *and* $\mathcal{E}_{i,w}^n = \frac{\alpha}{Re}\int_\Omega f_{i,w}^n d\boldsymbol{x}$.

*Proof.* Multiplying the first equation in system (26) by $\Delta t\mathbf{u}^{n+\frac{1}{2}}$ gives

$$
\begin{aligned}
&\int_\Omega \frac{1}{2}((\mathbf{u}^{n+1})^2 - (\mathbf{u}^n)^2)d\boldsymbol{x} + \int_\Omega \Delta t\mathbf{u}^{n+\frac{1}{2}}\cdot((\mathbf{u}^{n+\frac{1}{2}}\nabla)\cdot\mathbf{u}^{n+\frac{1}{2}})d\boldsymbol{x}\\
&-\frac{\Delta t}{Re}\int_\Omega P^{n+\frac{1}{2}}\nabla\cdot\mathbf{u}^{n+\frac{1}{2}}d\boldsymbol{x}\\
=\ &-\frac{\Delta t}{Re}\int_\Omega \nabla\mathbf{u}^{n+\frac{1}{2}} : \eta^n(\nabla\mathbf{u}^{n+\frac{1}{2}} + (\nabla\mathbf{u}^{n+\frac{1}{2}})^T)d\boldsymbol{x} + \frac{\Delta t}{Re}\sum_i\int_\Omega \mathbf{u}^{n+\frac{1}{2}}\cdot\nabla\phi_i^{n+1}\mu_i^{n+1}d\boldsymbol{x}\\
&-\frac{\Delta t}{Re}\sum_i\int_\Omega \lambda_i\delta_{\epsilon_i}\mathcal{P}_i^n : \nabla\mathbf{u}^{n+\frac{1}{2}}d\boldsymbol{x} + \frac{\Delta t}{Re}\sum_i\int_{\partial\Omega_w}\lambda_i^{n+\frac{1}{2}}(\delta_{\epsilon_i}\mathcal{P}_i^n\cdot\mathbf{n})\cdot\mathbf{u}_\tau^{n+\frac{1}{2}}ds\\
&+\frac{\Delta t}{Re}\int_{\partial\Omega_w}\mathbf{u}^{n+\frac{1}{2}}\cdot\eta^n((\nabla\mathbf{u}^{n+\frac{1}{2}} + (\nabla\mathbf{u}^{n+\frac{1}{2}})^T)\cdot\boldsymbol{n})ds\ . \qquad (32)
\end{aligned}
$$

Multiplying the fourth equation in system 26 by $\frac{\phi_i^{n+1}-\phi_i^n}{Re}$ and integration by parts lead to

$$
\begin{aligned}
&\frac{1}{Re}\sum_i\int_\Omega \mu_i^{n+1/2}(\phi_i^{n+1}-\phi_i^n)d\boldsymbol{x}\\
=\ &\frac{\kappa_B}{Re}\sum_i\int_\Omega\frac{1}{2\epsilon}((f_i^{n+1})^2 - (f_i^n)^2)d\boldsymbol{x} + \frac{\mathcal{M}_s}{Re}\frac{(S(\phi_i^{n+1})-S_{i,0})^2 - (S(\phi_i^n)-S_{i,0})^2}{2S_{i,0}}\\
&+\frac{\alpha}{Re}\sum_i\int_\Omega(H_i^{n+1}-H_i^n)d\boldsymbol{x} + \frac{\alpha}{Re}\sum_i\int_\Omega(f_w(\phi_i^{n+1}) - f_w(\phi_i^n))d\boldsymbol{x} \qquad (33)\\
&-\frac{\kappa_B}{Re}\sum_i\int_{\partial\Omega_w}\partial_n f_i^{n+\frac{1}{2}}(\phi_i^{n+1}-\phi_i^n)ds\\
&-\frac{\mathcal{M}_s}{Re}\sum_i\int_{\partial\Omega_w}\frac{S(\phi_i^{n+\frac{1}{2}})-S_{i,0}}{S_{i,0}}\epsilon\partial_n\phi_i^{n+\frac{1}{2}}(\phi_i^{n+1}-\phi_i^n)ds\ .
\end{aligned}
$$

Multiplying the third equation in system (26) by $\frac{\mu_i^{n+\frac{1}{2}}\Delta t}{Re}$ yields

$$
\begin{aligned}
&\frac{1}{Re}\sum_i\int_\Omega\mu_i^{n+\frac{1}{2}}(\phi_i^{n+1}-\phi_i^n)d\boldsymbol{x} + \frac{\Delta t}{Re}\sum_i\int_\Omega\mu_i^{n+\frac{1}{2}}(\mathbf{u}^{n+\frac{1}{2}}\cdot\nabla)\phi_i^{n+\frac{1}{2}}d\boldsymbol{x}\\
=\ &-\frac{\mathcal{M}\Delta t}{Re}\sum_i\int_\Omega(\nabla\mu_i^{n+\frac{1}{2}})^2d\boldsymbol{x}\ . \qquad (34)
\end{aligned}
$$

Multiplying the last equation in system (26) by $\frac{\lambda^{n+\frac{1}{2}}\Delta t}{Re}$ and integration by parts then sum by $i$ give

$$
\frac{\Delta t}{Re}\sum_i\int_\Omega(\lambda_i^{n+\frac{1}{2}}\delta_{\epsilon_i}\mathcal{P}_i^n) : \nabla\mathbf{u}^{n+\frac{1}{2}}d\boldsymbol{x} - \frac{\Delta t}{Re}\sum_i\int_\Omega\xi\epsilon^2(\phi_i^n)^2\left|\nabla\lambda_i^{n+\frac{1}{2}}\right|^2 d\boldsymbol{x} = 0\ . \qquad (35)
$$

The discretized energy dissipation law (31) is obtained by combining Eqs. (32)-(35) and organizing the terms according to the boundary conditions $L(\phi_i)$ as shown in (27). □

The spatial discretization using $C^0$ finite element is straight forward. Let $\Omega$ be the domain of interest with a Lipschitz-continuous boundary $\partial\Omega$. Let ${\mathbf{W}_b}^h \subset \mathbf{W}_b$ be a finite element space with respect to the triangulation of the domain $\Omega$. The fully discrete scheme of the system is to find

$$\left(\{\Phi_h\}^{n+1}, \{\boldsymbol{U}\}_h^{n+1}, \{F_h\}^{n+1}, \{\Lambda_h\}^{n+1}, \{p_h\}^{n+1}, \{\mathbf{u}_h\}^{n+1}\right) \in \mathbf{W}_b^h,$$

such that for any $(\psi_{1,h}, ..., \psi_{N,h}, \chi_{1,h}, ..., \chi_{N,h}, \zeta_{1,h}, ..., \zeta_{N,h}, \Theta_{1,h}, ..., \Theta_{N,h}, q_h, \mathbf{v}_h) \in \mathbf{W}_b^h$, the following scheme holds.

$$\begin{cases}
\int_\Omega \left( \frac{\mathbf{u}_h^{n+1} - \mathbf{u}_h^n}{\Delta t} + (\mathbf{u}_h^{n+\frac{1}{2}} \cdot \nabla)\mathbf{u}_h^{n+\frac{1}{2}} + \frac{1}{Re}\nabla P_h^{n+\frac{1}{2}} \right) \cdot \mathbf{v}_h d\boldsymbol{x} \\
= -\int_\Omega \frac{1}{Re}(\eta_h^n(\nabla \mathbf{u}_h^{n+\frac{1}{2}} + (\nabla \mathbf{u}_h^{n+\frac{1}{2}})^T)) : \nabla \mathbf{v}_h d\boldsymbol{x} \\
\qquad + \sum_i \int_\Omega \frac{1}{Re}\mu_{i,h}^{n+\frac{1}{2}} \nabla \phi_h^{n+\frac{1}{2}} \cdot \mathbf{v}_h d\boldsymbol{x} - \sum_i \int_\Omega \frac{1}{Re}\lambda_{i,h}^{n+\frac{1}{2}} \mathcal{P}_{i,h}^n \delta_{i,h,\epsilon} : \mathbf{v}_h d\boldsymbol{x} \\
\qquad + \int_{\partial\Omega_w} \frac{1}{Re}\mathbf{n} \cdot (\eta_h^n(\nabla \mathbf{u}_h^{n+\frac{1}{2}} + (\nabla \mathbf{u}_h^{n+\frac{1}{2}})^T) + \sum_i \lambda_{i,h}^{n+\frac{1}{2}} \mathcal{P}_{i,h}^n \delta_{i,\epsilon}) \cdot \mathbf{v}_h d\boldsymbol{x} \ , \\
\int_\Omega (\nabla \cdot \mathbf{u}_h^{n+\frac{1}{2}}) q_h d\boldsymbol{x} = 0 \ , \\
\int_\Omega (\frac{\phi_{i,h}^{n+1} - \phi_{i,h}^n}{\Delta t} + (\mathbf{u}_h^{n+\frac{1}{2}} \cdot \nabla)\phi_{i,h}^{n+\frac{1}{2}}) \psi_{i,h} d\boldsymbol{x} = -\int_\Omega \mathcal{M} \nabla \mu_{i,h}^{n+\frac{1}{2}} \nabla \psi_{i,h} d\boldsymbol{x} \ , \\
\int_\Omega \mu_{i,h}^{n+\frac{1}{2}} \chi_{i,h} d\boldsymbol{x} = \int_\Omega \Bigg( \kappa_B \frac{1}{\epsilon^2}((\phi_{i,h}^{n+1})^2 + (\phi_{i,h}^n)^2 + \phi_{i,h}^{n+1}\phi_{i,h}^n - 1) f_{i,h}^{n+\frac{1}{2}} \\
\qquad + \mathcal{M}_s \frac{(S(\phi_{i,h}^{n+\frac{1}{2}}) - S(\phi_{i,h,0}))}{S(\phi_{i,h,0})} (\frac{1}{4\epsilon}((\phi_{i,h}^{n+1})^2 + (\phi_{i,h}^n)^2 - 2)(\phi_{i,h}^{n+1} + \phi_{i,h}^n)) \Bigg) \chi_{i,h} d\boldsymbol{x} \\
\qquad + \int_\Omega (\kappa_B \nabla f_{i,h}^{n+\frac{1}{2}} + \mathcal{M}_s \epsilon \frac{(S(\phi_{i,h}^{n+\frac{1}{2}}) - S(\phi_{i,h,0}))}{S(\phi_{i,h,0})} \nabla \phi_{i,h}^{n+\frac{1}{2}}) \cdot \nabla \chi_{i,h} d\boldsymbol{x} \\
\qquad + \int_\Omega \alpha \frac{f_w(\phi_{i,h}^{n+1}) - f_w(\phi_{i,h}^n)}{\phi_{i,h}^{n+1} - \phi_{i,h}^n} \chi_{i,h} d\boldsymbol{x} + \int_\Omega \alpha \frac{(H_{i,h}^{n+1} - H_{i,h}^n)}{\phi_{i,h}^{n+1} - \phi_{i,h}^n} \chi_{i,h} d\boldsymbol{x} \\
\qquad - \int_{\partial\Omega_w} (\kappa_B \partial_{\mathbf{n}} f_{i,h}^{n+\frac{1}{2}} + \mathcal{M}_s \epsilon \frac{(S(\phi_{i,h}^{n+\frac{1}{2}}) - S(\phi_{i,h,0}))}{S(\phi_{i,h})} \partial_{\mathbf{n}} \phi_{i,h}^{n+\frac{1}{2}}) \chi_{i,h} ds \ , \\
\int_\Omega f_{i,h}^{n+\frac{1}{2}} \zeta_{i,h} = \int_\Omega \epsilon \nabla \phi_{i,h}^{n+\frac{1}{2}} \cdot \nabla \zeta_{i,h} + \int_\Omega \frac{1}{\epsilon}((\phi_{i,h}^{n+\frac{1}{2}})^2 - 1)\phi_{i,h}^{n+\frac{1}{2}} \zeta_{i,h} d\boldsymbol{x} \\
\qquad - \int_{\partial\Omega_w} \varepsilon \partial_{\mathbf{n}} \phi_{i,h}^{n+\frac{1}{2}} \zeta_{i,h} d\boldsymbol{x} \ , \\
\int_\Omega \delta_{i,h,\epsilon} \mathcal{P}_{i,h}^n : \nabla \mathbf{u}_{i,h}^{n+\frac{1}{2}} \Theta_{i,h} d\boldsymbol{x} - \int_\Omega \xi \epsilon^2 ((\phi_{i,h}^n)^2 \nabla \lambda_{i,h}^{n+\frac{1}{2}}) \cdot \nabla \Theta_{i,h} d\boldsymbol{x} \\
+ \int_{\partial\Omega_w} \xi \epsilon^2 ((\phi_{i,h}^n)^2 \partial_{\mathbf{n}} \lambda_{i,h}^{n+\frac{1}{2}}) \Theta_{i,h} d\boldsymbol{x} = 0 \ .
\end{cases}$$

Newton's iteration method is applied to solve the above nonlinear system. The unique solvability of (36) can be proved by following the approach introduced in [58].

# 4 Numerical Results

In this section, we first calibrate the model parameters and validate the model by comparing with the experimental data on RBC deformation under different stretching forces. Then cell-wall interaction simulations are used to study the effects of the cell-wall adhesion force and the local insensibility of cell membrane. The energy preservation of the numerical scheme is also illustrated.

Rest of this section is devoted to studying the cell aggregation and RBC motion when passing bifurcated blood vessel.

## 4.1 Convergence study

The temporal convergence rate of the scheme is tested here. The setting of this convergence study is shown in Figure 3. We place two cells next to each other initially. Due to the interaction potential $H$, motion and deformation of the cells occur, and the system gradually evolves to the steady state in which the two cells no longer move and deform.

The parameter values used for this simulation are chosen as follows: $Re = 2 \times 10^{-5}$, $\mathcal{M} = 5$, $\kappa_B = 2 \times 10^{-2}$, $\epsilon = 4 \times 10^{-2}$, $\mathcal{M}_s = 0$, $\alpha = 50$, $q_1 = 2$, $q_2 = 1$. The non-slip boundary condition is used for convenience. We take

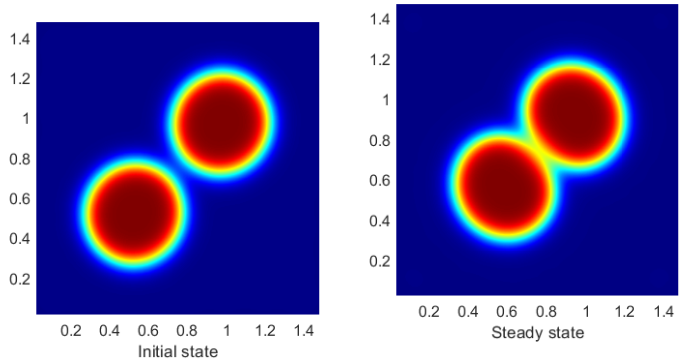


Figure 3: The initial and steady states of the temporal convergence test. Two cells are placed side by side with each other initially. As time evolves, these two cells adhere to form an aggregate, and show deformation at the steady state.

| Time step $\Delta t$ ($\times 10^{-6}$) | Error($u_x$) | Convergence Rate($u_x$) | Error($u_y$) | Convergence Rate($u_y$) | Error($\phi$) | Convergence Rate($\phi$) |
|---|---|---|---|---|---|---|
| 10.125 | 5.81e-4 | | 5.82e-4 | | 1.75e-3 | |
| 6.75 | 2.68e-4 | 1.90 | 2.68e-4 | 1.90 | 8.33e-4 | 1.83 |
| 4.5 | 1.16e-4 | 2.07 | 1.16e-4 | 2.07 | 3.76e-4 | 1.97 |
| 3 | 3.93e-5 | 2.67 | 3.93e-5 | 2.68 | 1.33e-4 | 2.58 |

Table 1: $L^2$ norm of the error and convergence rate for velocity $\mathbf{u} = (u_x, u_y)$, phase-field function $\phi$, at time $t = 3.24 \times 10^{-4}$ with both intercellular and extracellular fluid viscosities being 1.

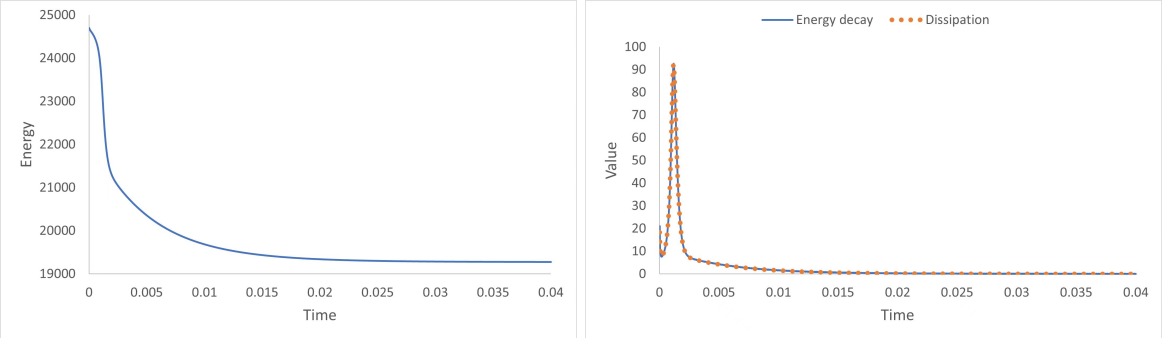


Figure 4: Energy dissipation law. Left: The evolution of discrete energy. Right: Scheme energy-law-preserving. Blue solid line: the energy change between each time step $\mathcal{E}_{total}^{n+1} - \mathcal{E}_{total}^{n}$; Red dots: the dissipation (RHS of Eq. (31) in each time step. The curves fit each other very well, which means that the energy-law-preserving law holds well.

the solution computed using $\Delta t = 2 \times 10^{-6}$ as the reference solution. The convergence result is shown in Table 1. Clearly, the discrete scheme is second-order accurate in time.

In Fig. 4, the results demonstrate the energy-law-preserving property of the scheme. The left panel provides evidence of energy decay over time. In the right panel, the blue solid line represents the energy change between each time step $\mathcal{E}_{total}^{n+1} - \mathcal{E}_{total}^{n}$, while the red dots correspond to the discrete dissipation (RHS of Eq. (31)). The plot confirms that the change of the discrete energy agrees with the energy law in Eq.(31), indicating that the proposed scheme is energy-law-preserving.

**Remark 4.1.** *In this case, we set the coefficient $\mathcal{M}_s$ to 0 in order to eliminate the possible effect on the convergence order from the $M_s$ related global term. In addition, this term is added for the purpose of keeping the total surface area constant. In the rest of the paper $\mathcal{M}_s$ is set to a nonzero value to preserve the surface area of the cell.*

**Remark 4.2.** *Here we only present the results of the temporal convergence test. The spatial convergence rate is also the second order, which is the same as that in [58]. The same $C^0$ finite element discretization is used in both this paper and [58].*

## 4.2 Benchmark: Red blood cell deformation under stretching force

Laboratory experiments have tested the non-linear elasticity and deformation of RBC [42] in which optical tweezers are used to provide stretching force to the cells. We set up a numerical simulation mimicking RBC deformation in the experiment. Here we take the top view of the cell, i.e., the circle shape, for 2D simulation. See the inset of Figure 5. In order to model the interaction between two optical tweezers and the RBC, $\phi_2$ in Eq. (9) is replaced by new phases $\phi_{tw_1}, \phi_{tw_2}$ to represent the two optical tweezers, respectively. The interaction energy thus becomes

$$H_{tw_i} = Q_{tw1}(\phi_1 + 1)^2(\phi_{tw_i} + 1)^2 - Q_{tw2}(\phi_1^2 - 1)^2(\phi_{tw_i}^2 - 1)^2 \ , \quad i = 1, 2 \ . \tag{36}$$

The force of the optical tweezers applied on the RBC is calculated by the following equation:

$$\mathbf{F} = \int_\Omega \frac{\partial H_{tw_i}}{\partial \phi} \nabla \phi d\boldsymbol{x} \ . \tag{37}$$

Values of other parameters used here are as follows: $Re = 2 \times 10^{-4}, \mathcal{M} = 0.25, \kappa_B = 2 \times 10^{-3}, k = 2 \times 10^{-12}, l_s = 5 \times 10^{-3}, \mathcal{M}_s = 2$.

The curves of axial and transverse diameter versus stretching forces are shown in Figure 5 together with the experimental data (diamonds with bars) from [42]. The results show that our model fits the experimental data very well.

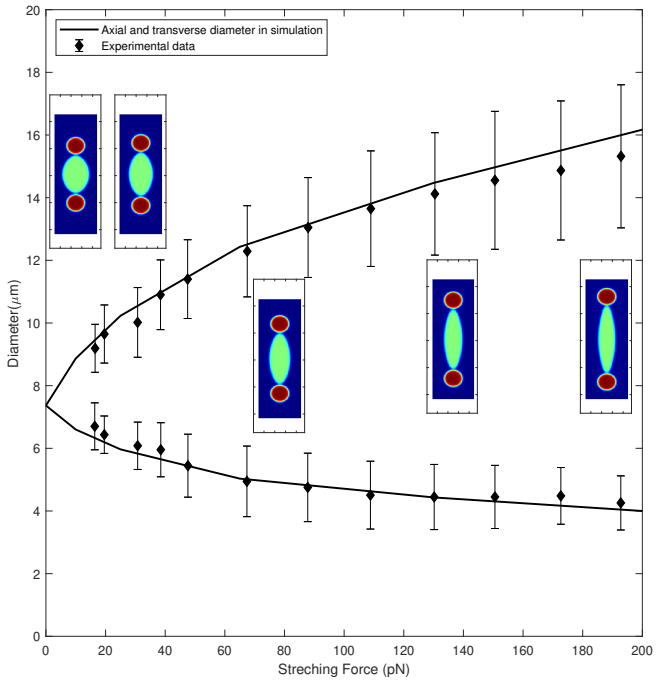


Figure 5: Nonlinear elastic deformation of red blood cells.The curve represents the relationship between diameter and stretching force. The diamonds on the curve represent the experimental data. In the experimental schematic diagram, the central phase represents the cell, and the surrounding regions on both sides represent the optical tweezers. The force applied to the membrane remains constant while the tweezers move. Equilibrium is reached when the membrane no longer extends under a specific stretching force.

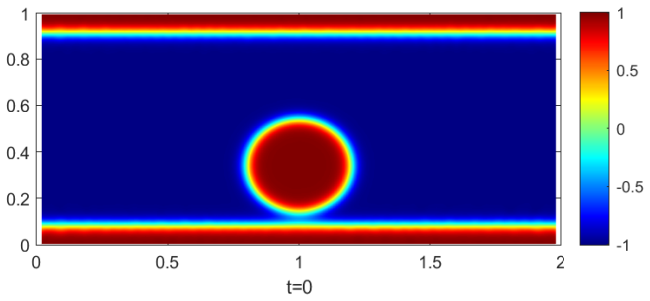


Figure 6: The initial condition for the test case of cell-wall attraction.

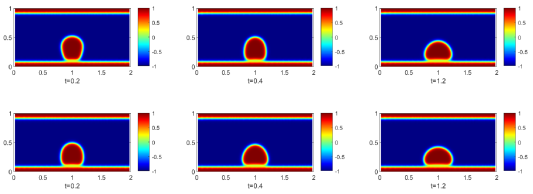

Figure 7: The top three pictures show the deformation of a cell with local inextensibility of its membrane; while the bottom three pictures show the deformation of a cell without the membrane local inextensibility at different times, respectively.

## 4.3 Cell-wall attraction

Cell-wall interaction under blood flow conditions plays important roles during blood clotting [64] and cancer cell invasion [20]. Simulation results presented in this section are used to investigate the effects of cell membrane local inextensibility and adhesion force on the cell-wall interaction. We first consider the effect of cell membrane local inextensibility using a 2D setting that a round cell is initially placed at a location with a point-wise contact with the wall boundary as shown in Figure 6. The parameter values of this simulation are listed as follows: $Re = 2\times10^{-4}, \mathcal{M} = 5\times10^{-4}, \kappa_B = 2\times10^{-2}, \varepsilon = 2\times10^{-3}, \mathcal{M}_s = 10^2, k = 4\times10^{-11}, l_s = 5\times10^{-6}, \alpha = 1000, q_{w_1} = 2, q_{w_2} = 1$.

Because of the cell-wall adhesion, the cell gradually develops a line that contacts with the wall. Snapshots of the cells modeled with and without local inextensibility of their membranes at different times are shown in Figure 7. We can clearly see that these two cells exhibit different dynamics in terms of changes in their shapes during cell-wall adhesion. As shown in Figure 8, the local inextensibility constraint impedes the deformation of the cell. For the cell modeled without the local inextensiblity constraint, the cell membrane attached to the wall is allowed to be stretched (red color in Figure 8) as well as compressed (blue color in Figure 8) to achieve the equilibrium faster. In contrast, the membrane of the cell modeled without local inextensibility displays almost no extensile or contractile phenomenon during the adhesion, which is consistent with experimental findings that lipid membrane is almost inextensible. Figure 9 shows that in both cases, the numerically computed energy of the two systems monotonously decays to the same value. It is also worth noting that the numerical energy of the system in which the cell is modeled without local inextensibility decays faster initially.

The effect of the strength of the adhesion force on the equilibrium profiles of the cells is illustrated in Figure 10. As expected, when the strength increases from 400 to 2500, the length of the cell-wall contact increases.

Competition between cell-wall adhesion and flow shear is studied in Figure 11. Many important subjects of study in biology involve this competition. E.g., free flowing platelets can adhere to inner surface of blood vessels when endothelial cell (EC) is altered or extracellular matrix substrates are exposed. This is a critical initial step in hemostasis and thrombosis. Recruitment of free flowing leukocytes to sites of inflammation is a key step in the body's innate immune response. This process is initiated by selectin-mediated leukocytes tethering and rolling along the EC surface, followed by integrin-dependent firm adhesion, prior to leukocytes extravasation into the tissue space [47]. Here we simulate two cells interacting with blood vessel wall under the shear flow condition. One cell is with strong adhesion force, and the other is with weak adhesion force with the vessel wall. Our simulations show that the cell with

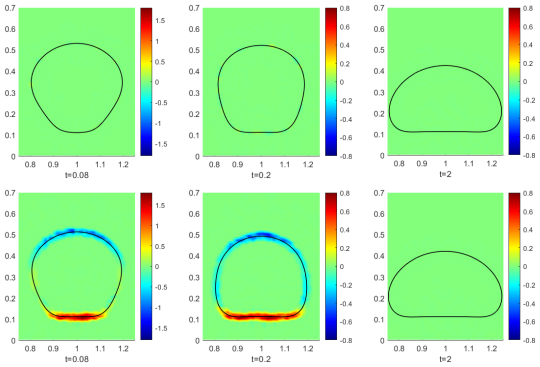


Figure 8: The top pictures show the values of surface divergence $\mathcal{P}_i : \nabla \mathbf{u}$ for the cell with membrane local inextensibility. The bottom pictures show the surface divergence of the cell without membrane local inextensibility.

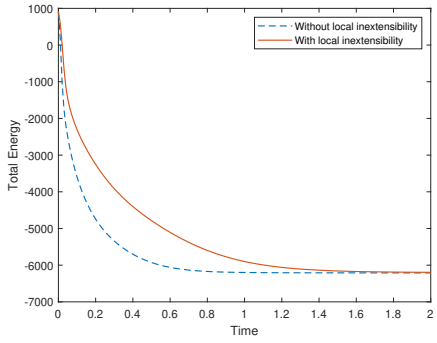


Figure 9: Total energy of the two system versus time.

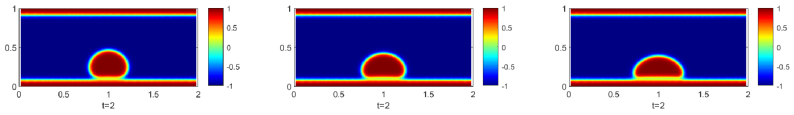


Figure 10: Equilibrium of the cells at different strengths of the adhesion force. (Left: $\alpha = 400$; Middle: $\alpha = 1000$; Right: $\alpha = 2500$.)

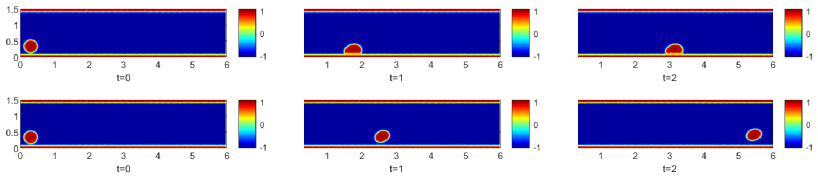


Figure 11: The top three picture shows the motion of the cell in strong adhesion case. The bottom three pictures shows the cell motion in weak adhesion case.

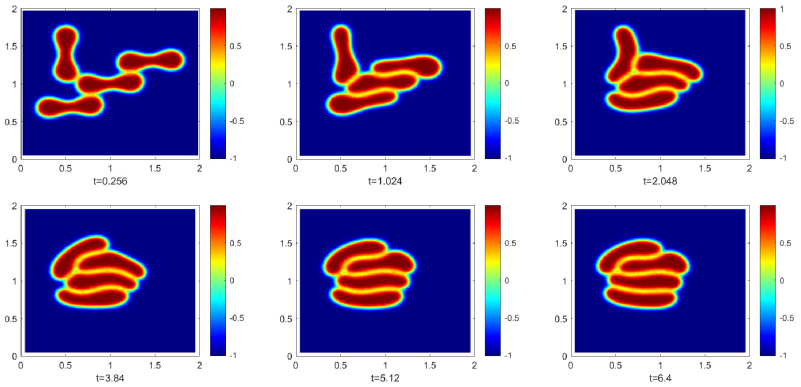


Figure 12: Aggregating of four red blood cells.

strong adhesion force is captured by the wall; while the cell with weak adhesion force is washed away by the shear flow. These are consistent with experimental observations. Nevertheless, note that our model is deterministic and uses a coarse-grained approach for modeling adhesion. This limits the capability of the model for studying stochastic effects of those selectin- or integrin-mediated adhesion.

## 4.4 Cell aggregation

Aggregation of RBCs is observed in experiment [35]. [54, 41] report that there is RBC hyperaggregatability phenomenon observed in Type 2 diabetes mellitus (T2DM) patients due to fibrinogen-dependent aggregation dynamics [10]. The hyperaggregatablility enhances the formation of rouleau [35] and [75], and subsequently leads to ischemic tissue [30]. In this section, we set up a simulation with four RBCs initially touching with each other at a small area of cell membranes. The parameter values are chosen to mimic real RBC and keep the adhesion force in the same range of tens to thousands of $pN$ as reported in [10, 59].

More specifically, the parameter values are: $Re = 2 \times 10^{-5}, \mathcal{M} = 5 \times 10^{-4}, \kappa_B = 4 \times 10^{-2}, k = 4 \times 10^{-12}, l_s = 5 \times 10^{-3}, \mathcal{M}_s = 10^3, \alpha = 3 \times 10^3, q_1 = 1, q_2 = 0.5$.

The evolution of this RBC system with time is shown in Figure 12. From the result we can see that RBCs creep together with respect to time under the attractive force, and form rouleaux. This is consistent with the experimental result shown in [35] and [75].

The deformation of the RBCs at equilibrium is related to the value of the attractive force [75, 76, 17]. Figure 13 shows clusters of RBCs with moderate and strong attractive (or aggregation) forces. The parameter values for simulations in Figure 13 are as follows: $Re = 2 \times 10^{-4}, \mathcal{M} = 5 \times 10^{-4}, \kappa_B = 2 \times 10^{-2}, k = 2 \times 10^{-11}, l_s = 5 \times 10^{-3}, \mathcal{M}_s = 10$.

From Figure 13, we can see that under strong aggregation force, obvious terminal hemispherical caps is shown and the offset between each adjacent cell is smaller as well. This result is consistent with the experimental observation [35].

In the following test, we place the RBCs in a Couette flow with flow shear rate being equal to $20s^{-1}$ with the

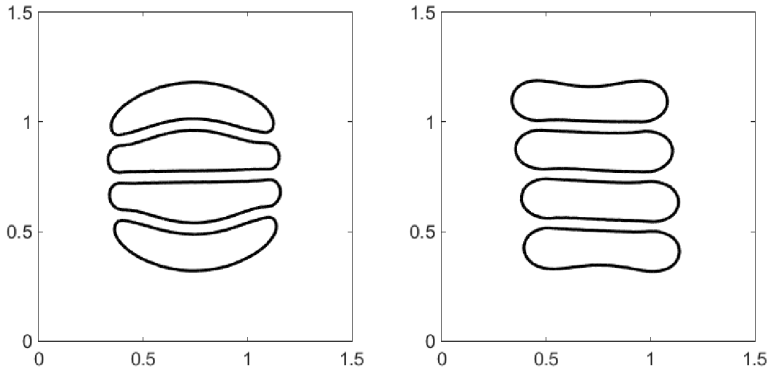


Figure 13: Left: Strong aggregate $\alpha = 15 \times 10^3, q_1 = 1, q_2 = 1$. Right: moderate aggregate $\alpha = 100, q_1 = 1, q_2 = 1$.

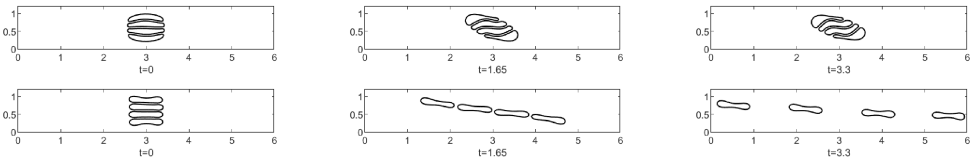


Figure 14: The top three figures shows the motion of the cells with strong aggregation. The bottom three figures shows the motion under moderate aggregation.

same dimension as in [74]. Motions of the cells are shown in Figure 14. Under shear flow, the rouleaux with strong adhesion force still aggregate together; while the one with weak adhesion force is broken up by the shear flow. This is consistent with the results reported in [74].

Now we simulate the motion of RBCs in branched vessels. Four RBCs are initially placed in the Y-shaped vessel. The width of the main channel (in which the inflow boundary condition is specified) of the Y-shaped vessel and the bottom branch of the vessel is set to be $1 \times 10^{-7}$ meters. The width of the top branch of the vessel is $0.7 \times 10^{-7}$ meters, which is close to the size of a red blood cell. A pressure drop boundary condition is used to introduce a shear flow in the vessel with a velocity around $5 \times 10^{-4} m/s$, which is close to the blood flow in capillaries. Other model parameter values in this simulation are as follows: $Re = 2 \times 10^{-4}, \mathcal{M} = 5 \times 10^{-4}, \kappa_B = 4 \times 10^{-2}, k = 4 \times 10^{-11}, l_s = 2 = 5 \times 10^{-6}, \mathcal{M}_s = 20$.

The motion of the RBCs and the velocity field of the flow are shown in Figures 15, 16 and 17, respectively. We first simulate the motion of the RBC group with a moderate aggregation force when they pass a Y-shaped channel with the same width of both branches as a baseline. The cells divide equally at the vessel bifurcation location. Then one of the channels is widened and a non-equal deviation is observed (3 move upwards,1 moves downward) due to the lower resistance in the upper branch. Then, under the same geometric setup, a strong aggregation force is applied to the cells. In this case, all RBCs go into the wider channel. The simulation result explains the experimental result in [35], in which a great number of RBCs are observed to be absent in the branched vessel under a strong aggregate case compared with moderate aggregate.

**Remark 4.3.** *In Figures 15, 16 and 17, the position and deformation of the cells and the distribution of the velocity field are both critical information that needs to be visualized. Thus we draw the cells with contour curves and the velocity field is marked with red arrows.*

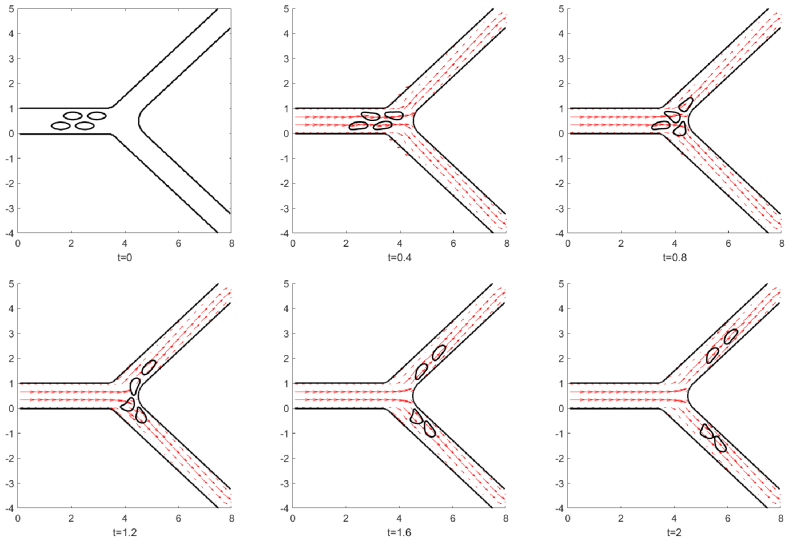


Figure 15: Cells are set in a cluster initially under a moderate aggregating force with $\alpha = 25, q_1 = 1, q_2 = 1$. The main channel width is 1 and the width of the two branches is 0.7. RBCs divide equally at the vessel bifurcation. The velocity field is indicated by the vector field.

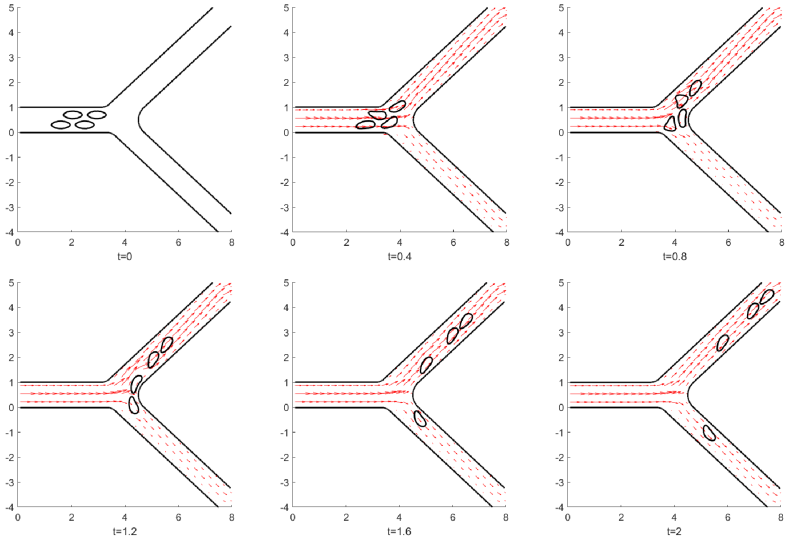


Figure 16: Cells are set in a cluster initially under a moderate aggregating force with $\alpha = 25, q_1 = 1, q_2 = 1$. The top branch is set to be 1 with the other stays 0.7. One of the cells is going into the branched vessel. The velocity field is shown as well.

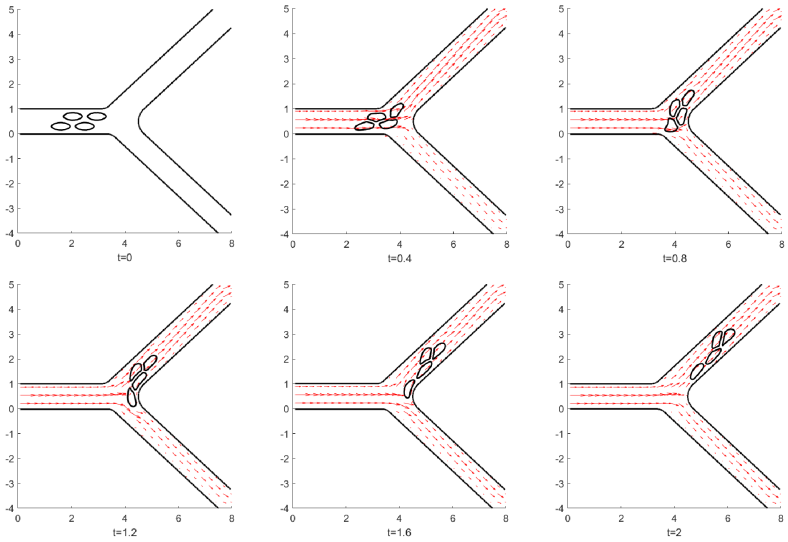


Figure 17: Cells are set in a cluster initially under a strong aggregating force with $\alpha = 1.5\times10^3, q_1 = 1, q_2 = 1$. The set up is the same as Figure 16. None of the cells is going into the branched vessel. The velocity field is shown as well.

# 5 Conclusions

In this paper, we have presented a thermodynamically consistent phase-field model for simulating cell deformation and aggregation, incorporating a new multi-dimensional Lennard-Jones type interaction energy that accounts for both repulsion and adhesion between cells and walls. The model's mechanical properties, including bending, surface area conservation, and local inextensibility, are modeled using different energy functionals.

We have proposed an efficient numerical scheme using $C^0$ finite element discretization in space and mid-point temporal discretization, which preserves energy unconditionally. The model and its parameters were calibrated and validated using experimental data on cell deformation under different stretch forces, and we have investigated the effects of adhesion strength on cell-wall and cell-cell interaction. The model was also used to study the motion of red blood cells near vessel bifurcations, which confirmed the role of hyperaggregability in inducing ischemic tissue in Type 2 diabetes mellitus patients.

It's important to note that while the Lennard-Jones potential provides a useful approximation for intermolecular interactions, cellular interactions are highly complex and involve a wide range of additional factors, such as specific cell adhesion molecules, signaling pathways, and mechanical properties. The Lennard-Jones type potential serves as a simplified representation to capture some aspects of cell interactions but may not fully capture the intricacies of biological systems. Future work will focus on extending the model to account for reaction and mass transportation on the membrane [51, 62], as well as studying the effects of T2DM on cell deformability and oxygen transportation. The model could also be combined with viscoelastic models [6, 68, 65] for vessels to simulate free-flowing red blood cells in narrow deformable vessels using the wall phase-field label $\phi_w$. Overall, this work offers a promising framework for simulating cell-cell and cell-wall interactions in complex flow conditions, with potential applications in biomedical engineering and pathology.

# Acknowledgments

This work was partially supported by the NSFC (grant numbers 12071190, 11771040, 11861131004, 91430106,12271492). L.S was partially supported by the Chinese Scholarship Council for studying at the University of Dundee. Z.X was partially supported by the NSF CDS&E-MSS 1854779.

# References


[1] Sebastian Aland et al. "Diffuse interface models of locally inextensible vesicles in a viscous fluid". In: *Journal of computational physics* 277 (2014), pp. 32–47.

[2] Yunus Alapan, Jane A Little, and Umut A Gurkan. "Heterogeneous red blood cell adhesion and deformability in sickle cell disease". In: *Scientific reports* 4.1 (2014), pp. 1–8.

[3] Ricard Alert and Xavier Trepat. "Physical models of collective cell migration". In: *Annual Review of Condensed Matter Physics* 11 (2020), pp. 77–101.

[4] D. M. Anderson, G. B. McFadden, and A. A. Wheeler. "DIFFUSE-INTERFACE METHODS IN FLUID MECHANICS". In: *Annual Review of Fluid Mechanics* 30.1 (1998), pp. 139–165. DOI: 10.1146/annurev.fluid.30.1.139. eprint: https://doi.org/10.1146/annurev.fluid.30.1.139. URL: https://doi.org/10.1146/annurev.fluid.30.1.139.

[5] Brian A Camley et al. "Polarity mechanisms such as contact inhibition of locomotion regulate persistent rotational motion of mammalian cells on micropatterns". In: *Proceedings of the National Academy of Sciences* 111.41 (2014), pp. 14770–14775.

[6] Suncica Canic et al. "Modeling viscoelastic behavior of arterial walls and their interaction with pulsatile blood flow". In: *SIAM Journal on Applied Mathematics* 67.1 (2006), pp. 164–193.

[7] Rui Chen et al. "Decoupled energy stable schemes for phase-field vesicle membrane model". In: *Journal of Computational Physics* 302 (2015), pp. 509–523.

[8] Qing Cheng and Jie Shen. "Multiple scalar auxiliary variable (MSAV) approach and its application to the phase-field vesicle membrane model". In: *SIAM Journal on Scientific Computing* 40.6 (2018), A3982–A4006.

[9] Yamicia Connor et al. "A mathematical model of tumor-endothelial interactions in a 3D co-culture". In: *Scientific reports* 9.1 (2019), pp. 1–14.

[10] Yixiang Deng et al. "Quantifying fibrinogen-dependent aggregation of red blood cells in type 2 diabetes mellitus". In: *Biophysical journal* 119.5 (2020), pp. 900–912.

[11] Qiang Du and Jian Zhang. "Adaptive finite element method for a phase field bending elasticity model of vesicle membrane deformations". In: *SIAM Journal on Scientific Computing* 30.3 (2008), pp. 1634–1657.

[12] Qiang Du et al. "A phase field formulation of the Willmore problem". In: *Nonlinearity* 18.3 (2005), p. 1249.

[13] Qiang Du et al. "Modeling the spontaneous curvature effects in static cell membrane deformations by a phase field formulation". In: *Communications on Pure & Applied Analysis* 4.3 (2005), p. 537.

[14] Qiang Du et al. "Energetic variational approaches in modeling vesicle and fluid interactions". In: *Physica D: Nonlinear Phenomena* 238.9-10 (2009), pp. 923–930.

[15] Bob Eisenberg, Yunkyong Hyon, and Chun Liu. "Energy variational analysis of ions in water and channels: Field theory for primitive models of complex ionic fluids". In: *The Journal of Chemical Physics* 133.10 (2010), p. 104104.

[16] Dmitry A Fedosov, Hiroshi Noguchi, and Gerhard Gompper. "Multiscale modeling of blood flow: from single cells to blood rheology". In: *Biomechanics and modeling in mechanobiology* 13.2 (2014), pp. 239–258.

[17] Daniel Flormann et al. "The buckling instability of aggregating red blood cells". In: *Scientific reports* 7.1 (2017), pp. 1–10.

[18] Aaron L Fogelson and Robert D Guy. "Immersed-boundary-type models of intravascular platelet aggregation". In: *Computer methods in applied mechanics and engineering* 197.25-28 (2008), pp. 2087–2104.

[19] Aaron L Fogelson and Keith B Neeves. "Fluid mechanics of blood clot formation". In: *Annual review of fluid mechanics* 47 (2015), pp. 377–403.

[20] Alf Gerisch and Mark AJ Chaplain. "Mathematical modelling of cancer cell invasion of tissue: local and non-local models and the effect of adhesion". In: *Journal of Theoretical Biology* 250.4 (2008), pp. 684–704.

[21] Mi-Ho Giga, A. Kirshtein, and Chun Liu. "Variational Modeling and Complex Fluids". In: 2017.

[22] Rui Gu, Xiaoqiang Wang, and M Gunzburger. "Simulating vesicle–substrate adhesion using two phase field functions". In: *Journal of Computational Physics* 275 (2014), pp. 626–641.

[23] Rui Gu, Xiaoqiang Wang, and Max Gunzburger. "A two phase field model for tracking vesicle–vesicle adhesion". In: *Journal of mathematical biology* 73.5 (2016), pp. 1293–1319.

[24] Francisco Guillén-González and Giordano Tierra. "Unconditionally energy stable numerical schemes for phase-field vesicle membrane model". In: *Journal of computational physics* 354 (2018), pp. 67–85.

[25] Zhenlin Guo and Ping Lin. "A thermodynamically consistent phase-field model for two-phase flows with thermocapillary effects". In: *Journal of Fluid Mechanics* 766 (2015), pp. 226–271.

[26] Zhenlin Guo, Ping Lin, and John S Lowengrub. "A numerical method for the quasi-incompressible Cahn–Hilliard–Navier–Stokes equations for variable density flows with a discrete energy law". In: *Journal of Computational Physics* 276 (2014), pp. 486–507.

[27] Zhenlin Guo, Ping Lin, and John S Lowengrub. "A numerical method for the quasi-incompressible Cahn–Hilliard–Navier–Stokes equations for variable density flows with a discrete energy law". In: *Journal of Computational Physics* 276 (2014), pp. 486–507.

[28] Zhenlin Guo et al. "A diffuse domain method for two-phase flows with large density ratio in complex geometries". In: *Journal of Fluid Mechanics* 907 (2021).

[29] Peter Höök et al. "Strong binding of platelet integrin $\alpha$IIb$\beta$3 to fibrin clots: Potential target to destabilize thrombi". In: *Scientific reports* 7.1 (2017), pp. 1–8.

[30] Kiave Yune Howangyin and Jean-Sébastien Silvestre. "Diabetes mellitus and ischemic diseases: molecular mechanisms of vascular repair dysfunction". In: *Arteriosclerosis, thrombosis, and vascular biology* 34.6 (2014), pp. 1126–1135.

[31] Dan Hu, Pingwen Zhang, and E Weinan. "Continuum theory of a moving membrane". In: *Physical Review E* 75.4 (2007), p. 041605.

[32] Yunkyong Hyon, Chun Liu, et al. "Energetic variational approach in complex fluids: maximum dissipation principle". In: *Discrete & Continuous Dynamical Systems* 26.4 (2010), p. 1291.

[33] J Jiang, K Garikipati, and S Rudraraju. "A diffuse interface framework for modeling the evolution of multi-cell aggregates as a soft packing problem driven by the growth and division of cells". In: *Bulletin of mathematical biology* 81.8 (2019), pp. 3282–3300.

[34] Kinneret Keren. "Cell motility: the integrating role of the plasma membrane". In: *European Biophysics Journal* 40.9 (2011), pp. 1013–1027.

[35] Thomas Kirschkamp et al. "Effects of Fibrinogen and $\alpha$2-Macroglobulin and Their Apheretic Elimination on General Blood Rheology and Rheological Characteristics of Red Blood Cell Aggregates". In: *Therapeutic Apheresis and Dialysis* 12.5 (2008), pp. 360–367.

[36] Kisung Lee et al. "Optical tweezers study of red blood cell aggregation and disaggregation in plasma and protein solutions". In: *Journal of biomedical optics* 21.3 (2016), p. 035001.

[37] Yaling Liu and Wing Kam Liu. "Rheology of red blood cell aggregation by computer simulation". In: *Journal of Computational Physics* 220.1 (2006), pp. 139–154.

[38] EC Löwenberg, JC Meijers, and M Levi. "Platelet-vessel wall interaction in health and disease." In: *The Netherlands journal of medicine* 68.6 (2010), pp. 242–251.

[39] J. Lowengrub and L. Truskinovsky. "Quasi-incompressible Cah-Hilliard fluids and topological transitions". en. In: *Proceedings of the Royal Society of London. Series A: Mathematical, Physical and Engineering Sciences* 454.1978 (Oct. 1998), pp. 2617–2654. ISSN: 1471-2946. DOI: 10.1098/rspa.1998.0273.

[40] Wieland Marth, Sebastian Aland, and Axel Voigt. "Margination of white blood cells: a computational approach by a hydrodynamic phase field model". In: *Journal of Fluid Mechanics* 790 (2016), pp. 389–406.

[41] Donald E McMillan. "The effect of diabetes on blood flow properties". In: *Diabetes* 32.Supplement_2 (1983), pp. 56–63.

[42] JP Mills et al. "Nonlinear elastic and viscoelastic deformation of the human red blood cell with optical tweezers". In: *Molecular & Cellular Biomechanics* 1.3 (2004), p. 169.

[43] CE Morris and Ulrike Homann. "Cell surface area regulation and membrane tension". In: *The Journal of membrane biology* 179.2 (2001), pp. 79–102.

[44] Makiko Nonomura. "Study on multicellular systems using a phase field model". In: *PloS one* 7.4 (2012), e33501.

[45] Lars Onsager. "Reciprocal relations in irreversible processes. I." In: *Phys. Rev.* 37.4 (1931), p. 405.

[46] Lars Onsager. "Reciprocal relations in irreversible processes. II." In: *Phys. Rev.* 38.12 (1931), p. 2265.

[47] Parag Pawar et al. "Roles of cell and microvillus deformation and receptor-ligand binding kinetics in cell rolling". In: *American Journal of Physiology-Heart and Circulatory Physiology* 295.4 (2008). PMID: 18660437, H1439–H1450. DOI: 10.1152/ajpheart.91536.2007. URL: https://doi.org/10.1152/ajpheart.91536.2007.

[48] Charles S Peskin. "Flow patterns around heart valves: A numerical method". In: *Journal of Computational Physics* 10.2 (1972), pp. 252–271. ISSN: 0021-9991. DOI: https://doi.org/10.1016/0021-9991(72)90065-4. URL: https://www.sciencedirect.com/science/article/pii/0021999172900654.

[49] Charles S. Peskin. "The immersed boundary method". In: *Acta Numerica* 11 (2002), pp. 479–517. DOI: 10.1017/S0962492902000077.

[50] Tiezheng Qian, Xiao-Ping Wang, and Ping Sheng. "A variational approach to moving contact line hydrodynamics". en. In: *Journal of Fluid Mechanics* 564 (Oct. 2006), p. 333. ISSN: 0022-1120, 1469-7645. DOI: 10.1017/S0022112006001935.

[51] Yuzhe Qin et al. "A phase field model for mass transport with semi-permeable interfaces". In: *Journal of Computational Physics* (2022), p. 111334.

[52] Bryan Quaife, Shravan Veerapaneni, and Y-N Young. "Hydrodynamics and rheology of a vesicle doublet suspension". In: *Physical Review Fluids* 4.10 (2019), p. 103601.

[53] Bryan Quaife, Shravan Veerapaneni, and Y-N Young. "Hydrodynamics and rheology of a vesicle doublet suspension". In: *Physical Review Fluids* 4.10 (2019), p. 103601.

[54] H Schmid-Schönbein and E Volger. "Red-cell aggregation and red-cell deformability in diabetes." In: *Diabetes* 25.2 SUPPL (1976), pp. 897–902.

[55] Jie Shen, Jie Xu, and Jiang Yang. "The scalar auxiliary variable (SAV) approach for gradient flows". In: *Journal of Computational Physics* 353 (2018), pp. 407–416.

[56] Jie Shen and Xiaofeng Yang. "The IEQ and SAV approaches and their extensions for a class of highly nonlinear gradient flow systems". In: *Contemp. Math* 754 (2020), pp. 217–245.

[57] Lingyue Shen et al. "An energy stable C0 finite element scheme for a quasi-incompressible phase-field model of moving contact line with variable density". In: *Journal of Computational Physics* 405 (2020), p. 109179.

[58] Lingyue Shen et al. "An Energy Stable C^0 Finite Element Scheme for A Phase-Field Model of Vesicle Motion and Deformation". In: *SIAM Journal on Scientific Computing* 44.1 (2022), B122–B145.

[59] Patrick Steffen, Claude Verdier, and Christian Wagner. "Quantification of depletion-induced adhesion of red blood cells". In: *Physical review letters* 110.1 (2013), p. 018102.

[60] Jan Steinkuhler et al. "Mechanical properties of plasma membrane vesicles correlate with lipid order, viscosity and cell density". In: *Communications biology* 2.1 (2019), pp. 1–8.

[61] Denisa D Wagner and Paul S Frenette. "The vessel wall and its interactions". In: *Blood, The Journal of the American Society of Hematology* 111.11 (2008), pp. 5271–5281.

[62] Xiaolong Wang et al. "An immersed boundary method for mass transfer through porous biomembranes under large deformations". In: *Journal of Computational Physics* (2020), p. 109444.

[63] Thomas R Weikl et al. "Adhesion of membranes via receptor–ligand complexes: Domain formation, binding cooperativity, and active processes". In: *Soft Matter* 5.17 (2009), pp. 3213–3224.

[64] Ziheng Wu et al. "Three-dimensional multi-scale model of deformable platelets adhesion to vessel wall in blood flow". In: *Philosophical Transactions of the Royal Society A: Mathematical, Physical and Engineering Sciences* 372.2021 (2014), p. 20130380.

[65] Shixin Xu, Mark Alber, and Zhiliang Xu. "Three-phase Model of Visco-elastic Incompressible Fluid Flow and its Computational Implementation". In: *Communications in Computational Physics.* 25(2) (2019), pp. 586–624.

[66] Shixin Xu, Mark Alber, and Zhiliang Xu. "Three-phase model of visco-elastic incompressible fluid flow and its computational implementation". In: *Communications in computational physics* 25.2 (2019), p. 586.

[67] Shixin Xu, Ping Sheng, and Chun Liu. "An energetic variational approach for ion transport". In: *Communications in Mathematical Sciences* 12.4 (2014), pp. 779–789.

[68] Shixin Xu et al. "Model predictions of deformation, embolization and permeability of partially obstructive blood clots under variable shear flow". In: *Journal of the Royal Society, Interface* 14.136 (2017). ISSN: 1742-5662. DOI: 10.1098/rsif.2017.0441.

[69] Shixin Xu et al. "Osmosis through a semi-permeable membrane: a consistent approach to interactions". In: *arXiv preprint arXiv:1806.00646* (2018).

[70] Zhiliang Xu et al. "Study of blood flow impact on growth of thrombi using a multiscale model". In: *Soft Matter* 5.4 (2009), pp. 769–779.

[71] Xiaofeng Yang, Vladimir Mironov, and Qi Wang. "Modeling fusion of cellular aggregates in biofabrication using phase field theories". In: *Journal of theoretical biology* 303 (2012), pp. 110–118.

[72] Xiaofeng Yang, Jia Zhao, and Qi Wang. "Numerical approximations for the molecular beam epitaxial growth model based on the invariant energy quadratization method". In: *Journal of Computational Physics* 333 (2017), pp. 104–127.

[73] Jian Zhang, Sovan Das, and Qiang Du. "A phase field model for vesicle–substrate adhesion". In: *Journal of Computational Physics* 228.20 (2009), pp. 7837–7849.

[74] Junfeng Zhang, Paul C Johnson, and Aleksander S Popel. "Red blood cell aggregation and dissociation in shear flows simulated by lattice Boltzmann method". In: *Journal of biomechanics* 41.1 (2008), pp. 47–55.

[75] Primoz Ziherl. "Aggregates of two-dimensional vesicles: Rouleaux, sheets, and convergent extension". In: *Physical review letters* 99.12 (2007), p. 128102.

[76] Primoz Ziherl and Sasa Svetina. "Flat and sigmoidally curved contact zones in vesicle–vesicle adhesion". In: *Proceedings of the National Academy of Sciences* 104.3 (2007), pp. 761–765.